JOURNAL OF PROPULSION AND POWER
Vol. 39, No. 4, July–August 2023

Check for updates

Effects of Thermal/Chemical Nonequilibrium on a High-Mach Ethylene-Fueled Scramjet

Wei Yao,* Hang Liu,† Zheng Zhang,‡ Xu Zhang,§ Lianjie Yue,¶ Xiaoyuan Zhang,** and Jinping Li††
Institute of Mechanics, Chinese Academy of Sciences, 100190 Beijing, People's Republic of China

https://doi.org/10.2514/1.B39007

An ethylene-fueled scramjet operating at Mach 10 was experimentally tested in the JF-24 shock tunnel and modeled using improved delayed detached eddy simulation based on up to 368.34 million cells. An in-depth analysis of the effects of thermal and chemical nonequilibrium on combustion characteristics and engine performance was conducted. The contrary effects of nonequilibrium heating and nonequilibrium cooling that occur in different sections of a scramjet were revealed. The underlying mechanism can be attributed to the delayed relaxation of thermal nonequilibrium under energy addition or deduction. The nonequilibrium case has better mixing, while the equilibrium case has higher combustion efficiency. The synchronous reductions in thrust and drag counteract each other and lead to a higher final net thrust under nonequilibrium. The net thrust increases with the global equivalence ratio, whereas the specific impulse decreases. The evolution of flamelets and reaction paths were analyzed to reveal the effect of chemical nonequilibrium, which produces an abundance of O, OH, and NO radicals through endothermic dissociation reactions and significantly alters the rate-limiting reaction paths.

Downloaded by "Chinese Academy of Sciences (CAS), Institute of Mechanics" on April 11, 2024 | http://arc.aiaa.org | DOI: 10.2514/1.B39007

Nomenclature

A_s, B_s	=	species-related coefficients in the vibrational-translational relaxation time model
C_p	=	specific heat at constant pressure, J/(kg · K)
C_{DES}	=	empirical constant in Detached-Eddy Simulation, 0.65
C_d	=	model constant, 2.0
C_g	=	model constant, 2.86
C_k	=	turbulence model constant, 0.07
c	=	reaction progress variable
D'	=	dissociation energy, J/kg
D_T	=	thermal diffusivity, m^2/s
D_α, D_ξ	=	mass diffusivities of species α and mixture fraction ξ, m^2/s
d	=	wall distance, m
d_{IDDES}	=	length scale in improved delayed detached eddy simulation, m
E_a	=	activation energy, J/kg
E_d	=	dissociation energy, J/kg
e_{el}	=	electronic energy, J/kg
H	=	flight altitude, km
H_0	=	stagnation enthalpy, MJ/kg
H, H^0, H_t	=	absolute enthalpy, formation enthalpy, and total absolute enthalpy, J/kg
H_{tr},	=	transrotational and vibrational–electron–electronic energy, J/kg
k_{eq}	=	equilibrium chemical rate
k	=	turbulent kinetic energy, m^2/s^2
k_{sgs}	=	subgrid-scale turbulent kinetic energy, m^2/s^2
L, M, N	=	numbers of species, reactions, and mesh cells
Ma	=	Mach number
M_η	=	conditional diffusion
$\dot{m}$	=	mass flow rates, kg/s
$\dot{m}_p$	=	phase change rate, kg/s
$P(\eta)$	=	probability density function with the independent variable η
Pr_t	=	turbulent Prandtl number
p, P_0	=	static and total pressure, Pa
Q_{CV}	=	vibrational–electronic energy source term in the coupled vibration–chemistry–vibration model, W/m^3
$Q_{l,\alpha}$	=	conditional liquid fuel composition
Q_{VT}	=	vibrational-translational energy exchange rate, W/m^3
Q_T	=	conditionally averaged temperature, K
Q_α	=	conditional mean of mass fraction for species α
q	=	dynamic pressure, kPa
R, R_u	=	gas constant (J/(kg · K)) and universal gas constant (≈8.314 J/(mol · K))
Re	=	Reynolds number
S_{ij}	=	strain rate tensor, m/s
Sc_t	=	turbulent Schmidt number
T, T_0	=	static temperature, and total temperature, K
T_{eff}	=	Park's overall temperature, K
T_t, T_v	=	transrotational and vibrational–electron–electronic temperature, K
T^0, T^*, T_Γ, T_U	=	pseudotemperatures in the coupled vibration–chemistry–vibration model
t	=	time, s
$\boldsymbol{U}$, U	=	velocity vector and magnitude, m/s
u_i, u_i'	=	the ith-component of velocity and its fluctuation, m/s
V	=	cell volume, mm^3
W_m, $W_{m,\alpha}$	=	molecular weight of the mixture and species α, g/mol
W_α	=	production rate of species α, s^{-1}
X_α	=	molecular fraction of species α
x	=	streamwise distance, m

Received 31 August 2022; revision received 26 December 2022; accepted for publication 28 December 2022; published online 19 January 2023. Copyright © 2023 by the American Institute of Aeronautics and Astronautics, Inc. All rights reserved. All requests for copying and permission to reprint should be submitted to CCC at www.copyright.com; employ the eISSN 1533-3876 to initiate your request. See also AIAA Rights and Permissions www.aiaa.org/randp.

*Professor, Key Laboratory of High-Temperature Gas Dynamics; also School of Engineering Science, University of Chinese Academy of Science, 100049 Beijing, People's Republic of China; weiyao@imech.ac.cn (Corresponding Author).

†Ph.D. Student, Key Laboratory of High-Temperature Gas Dynamics; liuhang@imech.ac.cn.

‡Assitant Professor, Key Laboratory of High-Temperature Gas Dynamics; zhangzheng@imech.ac.cn.

§Assitant Professor, Key Laboratory of High-Temperature Gas Dynamics; also School of Engineering Science, University of Chinese Academy of Science, 100049 Beijing, People's Republic of China; zhangxu@imech.ac.cn.

¶Professor, Key Laboratory of High-Temperature Gas Dynamics; yuelj@imech.ac.cn.

**Assitant Professor, Key Laboratory of High-Temperature Gas Dynamics; zhangxiaoyuan@imech.ac.cn.

††Associate Professor, Key Laboratory of High-Temperature Gas Dynamics; lijinping@imech.ac.cn.

Downloaded by "Chinese Academy of Sciences (CAS), Institute of Mechanics" on April 11, 2024 | http://arc.aiaa.org | DOI: 10.2514/1.B39007

x_i = Cartesian coordinate in the ith direction
$Y_{l,\alpha}$ = mass fraction of species α in the liquid phase
Y_α = mass fraction of species α
Y_α^0 = oxidizer stream composition
Y_α' = unconditional fluctuation of species α
Y_α'' = conditional fluctuation of species α
y^+ = nondimensional wall distance
α = species order
γ = energy fraction in the coupled vibration–chemistry–vibration model
Δ = local filter width of the subgrid turbulence, m
δ_{ij} = Kronecker delta function
ζ = parameter in the quasi-classical trajectory model
η = sample space for mixture fraction
ν, ν_{sgs} = kinematic viscosity and subgrid-scale viscosity, m^2/s
ξ_{st} = stoichiometric mixture fraction
$\tilde{\xi}$, $\widetilde{\xi''^2}$ = mean and variance of mixture fraction
ξ_l = liquid composition expressed in mixture fraction
ρ = density, kg/m^3
ρ_η = conditional density, $\langle\rho|\eta\rangle$, kg/m^3
σ = model constant in vibrational-translational relaxation time model, 10^{-21} m^2
$\tilde{\tau}_{ij}$, τ_{ij} = viscous and Reynolds stress tensor, $\text{kg}/(\text{m}\cdot\text{s}^2)$
τ_{VT} = vibrational-translational relaxation time, s
ϕ = efficiency function in the coupled vibration–chemistry–vibration model
Φ = global fuel equivalence ratio
χ = scalar dissipation rate, s^{-1}
$\Psi_{T,j}$ = turbulent enthalpy flux, W/m^2
$\Psi_{\xi,j}$ = turbulent species diffusion, $\text{kg}/(\text{m}^2\cdot\text{s})$
ω = turbulence kinetic energy dissipation rate, m^2/s^3

Subscripts

air = air stream variables
fuel = fuel stream variables
i, j = vector components
zone = zone-based mean
α = species index

Superscripts

$\sim$ = Favre-averaged quantity
$-$ = averaged quantity

I. Introduction

THE terminology "hypersonic combustion" was first defined by Stalker [1,2] as the combustion that occurs under $Ma \geq 5$. The main characteristic of hypersonic combustion is that the heat released from combustion takes only a small percentage of the total flow enthalpy [2]. Consequently, the flow deflection and boundary separation due to heat addition is considered minor, and the flow exhibits a more hyperbolic pattern with weak "upstream interaction" [3]. Scramjet, also known as supersonic ramjet [4], is an airbreathing engine that burns fuel with supersonic atmospheric air. High-Mach scramjets (i.e., those designed to operate at $Ma \geq 8$) are usually characterized by hypersonic combustion inside the combustor, whose entrance airflow can reach hypersonic speed. Scramjet has the advantage of no requirement on carrying oxidizer onboard, thereby, a significantly higher specific impulse over rockets when used as a hypersonic booster. Flight tests using scramjets to achieve net thrust have been demonstrated to be feasible [5,6]. To be a suitable replacement for rockets as the second stage in the access-to-space system, scramjets capable of operating at $Ma \geq 8$ are desirable. However, the drag usually rises drastically with the flight Mach number, and it is not easy to achieve high combustion efficiency of over 80% [7] for a hypersonic combustor.

The research on hypersonic combustion has drawn more attention in recent years [8–11] to extend the operation limit of scramjets further. Scramjets operated at $Ma = 12$ have been numerically studied by Kodera et al. [12], Zhang et al. [13], and later by Liu et al. [11], who observed complicated diamond-shaped shock train structures in the high-temperature combustion region and emphasized the importance of shock-aided flame stabilization. Moura et al. [14] numerically reproduced a scramjet test under $Ma = 10$ conducted in the T4 Reflected Shock Tunnel and pointed out that the non-premixed combustion is more prevalent for the examined fuel-lean equivalence ratio of 0.13. The flow residence time significantly reduces under high-Mach conditions, resulting in severely incomplete mixing and combustion of the fuel. A common approach to improve combustion efficiency and flame stabilization is to increase the length of the combustor. For example, the combustor may become as long as 3–5 m for $Ma > 10$, dramatically increasing the wall skin friction and complicating the implementation of active cooling systems [15]. Various novel scramjet designs have been proposed and investigated to reduce the combustor length while improving the combustion performance under high-Mach conditions. The concept of wave combustor, i.e., shock-induced combustion ramjet (shcramjet), was proposed [16,17] and numerically shown to be capable of achieving high specific impulse for $Ma \geq 10$ [18,19]. Bricalli et al. [20] investigated the performance of a three-dimensional (3-D) nonuniform compression scramjet with premixed inflow under $Ma = 10$ and found that the 3-D flow–combustion interactions enabled the flame to be propagated into the low-compression region. Petty et al. [21] quantify the beneficial effects of oxygen enrichment for a Mach 12 scramjet. An airframe-integrated scramjets with a rectangular-to-elliptical shape-transition (REST) inlet operated at flight Ma 12 was examined by Barth [22] and Yao et al. [8,10]. Yao et al. [8] conducted a systematic performance analysis of a strut-aided scramjet operating over a wide range of flight conditions with $Ma = 7$–10.

One key feature of hypersonic combustion is that thermal/chemical nonequilibrium effects become prominent due to the increase in stagnation temperature and Knudsen number. Significant impacts on flow patterns and combustion characteristics when incorporating the nonequilibrium models have been observed [10,23–31]; however, nonequilibrium effects on engine performance under high-Mach conditions have been rarely evaluated in the literature. As pointed out in [10], most of the current nonequilibrium flow modelings focus on the external flow around hypersonic vehicles [28,30,32], while less attention has been paid to the internal flow of engines. More importantly, it is worth pointing out that not all the previous observations of nonequilibrium effects have been well understood, and the conclusions drawn from different studies may even seem inconsistent. The nonequilibrium was usually observed to cause a reduction in translational temperature (T_t) through energy transfer, i.e., the nonequilibrium cooling effect [10], which suppresses the chemical reactions and ulteriorly brings down the increasing rate of T_t. It seems that the presence of nonequilibrium inhibits combustion, leading to flame stabilization further downstream and may even flame blowout [29]. However, it was also observed [31] that the presence of nonequilibrium "counterintuitively" facilitates ignition and leads to flame stabilization at a more upstream location.

Growing interests [33–36] focused on scramjets fueled by hydrocarbons, which have higher calorific value and more convenient storability than hydrogen. However, the slow chemistry and complex reaction paths imply that the nonequilibrium effects should exert more influence on hydrocarbon-fueled hypersonic combustion, which has rarely been studied. A close examination would be required to reveal the underlying physical mechanisms and provide a unified explanation for those fragmented observations or seemingly contradictory conclusions drawn by different researchers. Such a unified rule can be more helpful in guiding the design of high-Mach airbreathing engines, which is the motivation of this study. The significant flow variations across the cross section demand a fully 3-D transient representation of the flowfield [37,38]; thus, a high-fidelity large-eddy simulation (LES) is used for the internal flow in

this study. The paper is organized as follows. Firstly, Sec. II presents the scramjet design and the experimental test. The physical models related to thermal/chemical nonequilibrium, turbulence, and combustion are then presented, together with the governing equations and computational configurations. The flowfields and engine performances are analyzed for different scramjet cases in Sec. III, where the evolution of flamelets and reaction paths are analyzed to reveal the underlying mechanisms of the nonequilibrium effects.

II. Physical Models and Computational Details

A. Experimental Case

The experiment was conducted in the JF-24 backward-detonation-driven pulse high-enthalpy shock tunnel [39,40], which uses reflected shock waves to compress the air in the driven section to be high pressure and high enthalpy. The backward detonation can produce a much more uniform yet time-stable driving gas, while the state of forward detonation driving gas decays quickly with time [41]. JF-24 consists of a shock tube, a Laval nozzle, a test section, and a vacuum chamber. Among them, the 23-m-long shock tube is composed of an explosion-damping section, a driving section, and a driven section, all separated by diaphragms. The operation process was illustrated in [42] for the detonation-driven shock tunnel operated in the backward-running detonation mode. The detonation of $H_2/O_2/N_2$ mixture initiated between the driving section and the driven section produces high-pressure gas to drive the air in the driven section. The nozzle flow starts once the incident shock is reflected at the end of the driven section. The reflected shock wave further compressed the test gas to be high-pressure, high-enthalpy, and stagnated. The Laval nozzle accelerates the shock-compressed air to be supersonic and then outputs it to the test section, where the tested scramjet was installed in a direct-connect way. The effective test time terminates when the reflected expansion wave from the driving section arrives at the end of the driven section.

Figure 1 shows the scramjet with the isolator directly connected to the JF-24 nozzle. The tested scramjet has no inlet section, whose compression effect was simulated by directly supplying a Mach 4.3 high-enthalpy flow to the isolator. JF-24 was designed to provide the capacity of reproducing flight conditions from Mach 9 to 15, with total temperature varying from 3000 to 6000 K and total pressure up to 20 MPa. The maximum operation time of JF-24 ranges from 5 to 16 ms, depending on the reference states. In the current study, the test gas issued from the JF-24 nozzle simulates the flight Mach of 10 at an altitude of 37 km, with a total temperature of 3843 K and a total pressure of 37.25 MPa. Note that, in the evaluation of total temperature and total pressure, the air dissociation effect has been taken into account. In the direct-connect facility, the total pressure loss by the inlet compression was simulated by assuming a total pressure recovery coefficient. The final static temperature and static pressure imposed at the entrance of the isolator are 1002 K and 31.7 kPa, respectively.

Figure 2 shows the schematics of the tested scramjet and the fuel injection section. The total length of the scramjet is 6.28 m, and part of the external flow with a length of 0.67 m is added into the computational domain to reproduce the inflow conditions accurately. A Cartesian coordinate system defining the streamwise direction as the x direction and locating the origin at the start point is established for the convenience of description. The 2.49-m-long inlet is designed by the streamline tracking method [43] with a viscous boundary-layer thickness correction based on the reference temperature method [44]. The geometric contraction ratio of the inlet is 10. The isolator section smoothly transits from the round inlet to the round combustor. The combustor uses a 0.985-m-long mildly expanded cone section to transit to a single-side expanded nozzle. The sweep angle of the trailing edge of the cavity is 46°. At the flight Mach number of 10, the

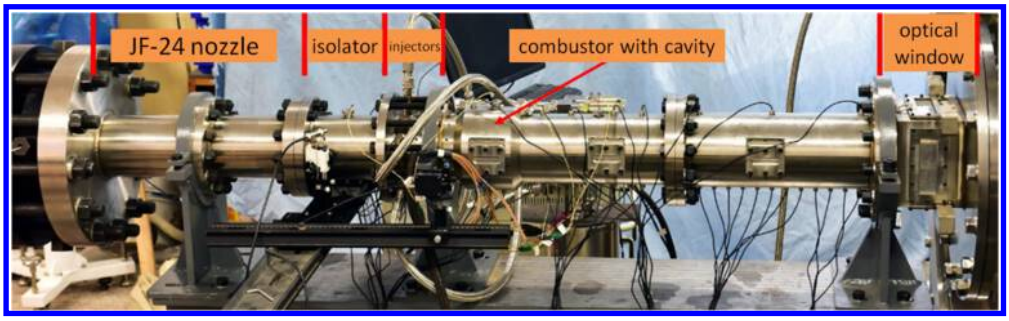

Fig. 1 The direct-connect scramjet tested in the JF-24 shock tunnel.

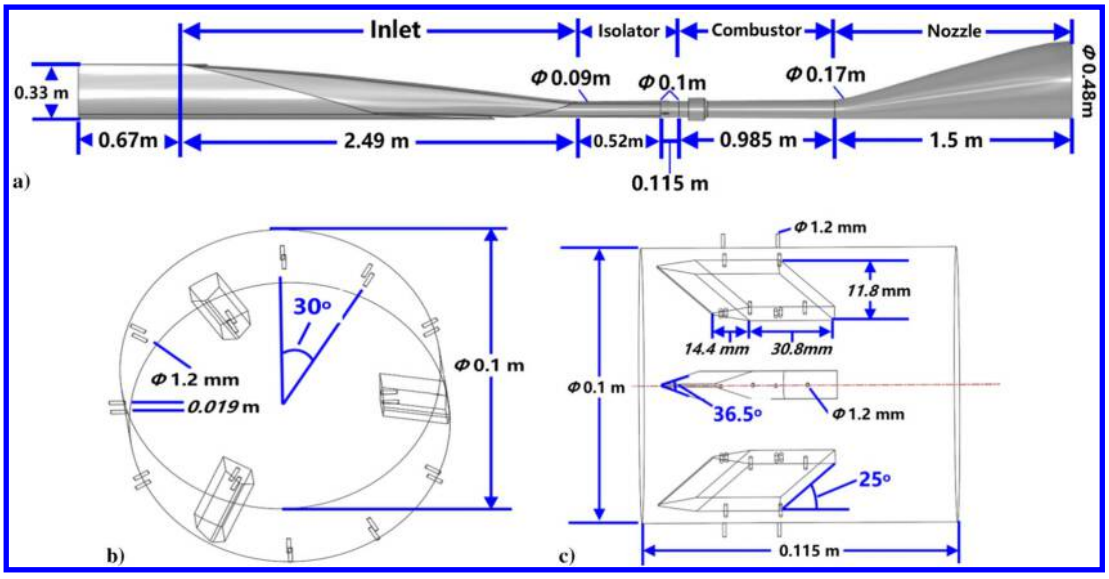

Fig. 2 Schematic of a) the scramjet with the external flow, b) pylon structures, and c) fuel injectors.

Downloaded by "Chinese Academy of Sciences (CAS), Institute of Mechanics" on April 11, 2024 | http://arc.aiaa.org | DOI: 10.2514/1.B39007

Table 1 Summary of the configuration parameters of the modeled cases

Air stream							Fuel (C_2H_4) stream			
			Y_{N2}: 0.767, Y_{O2}: 0.233				Y_{C2H4}: 1.0			
Ma	H, km	T, K	p, Pa	U, m/s	q, Pa	$\dot{m}_{air}$, kg/s	$\dot{m}_{fuel}$, kg/s	Φ	T_0, K	Ma
10	37	242	433	3,119	30,325	1.47	0.06 0.10 0.14	0.6 1.0 1.4	300	1

supersonic air crossflow in the combustor reaches hypersonic speed, resulting in a low jet-to-crossflow pressure ratio. Therefore struts are used to increase the jet penetration depth. Figure 2b shows that the fuel injection module is configured with three pylons evenly distributed in the circumferential direction. A cavity flame stabilizer is installed in the mildly expanded section, with the leading edge 60 mm downstream of the fuel injection module. The cavity surrounds the whole circumference of the combustor, with a depth of 20 mm and a length of 100 mm.

To examine the thermal/chemical nonequilibrium effects on hydrocarbon-fueled supersonic combustion, ethylene is selected as the test fuel in this study. Hydrocarbons are considered a more practical fuel for scramjets because of their distinctive advantages of high density and ease of use and maintenance [34,35,45–50]. As a highly reactive hydrocarbon fuel, ethylene is frequently adopted as the surrogate for endothermically cracked jet fuels [51,52]. Ethylene under different global equivalence ratios of 0.6, 1.0, and 1.4 is injected at the room temperature of 300 K. As shown in Fig. 2c, there are two dozens of 1.2-mm-diam injection portholes, with each two laid in a row. The rows of portholes are evenly distributed along the circumference of the combustor wall, with nine rows on the wall and three on the top of the pylons. All the portholes are injected perpendicular to the local wall surface.

Table 1 summarizes the parameters of the three modeled cases. The incoming flow simulates the flight condition at Mach 10 and an altitude of 37 km, where the ambient pressure and temperature are 433 Pa and 242 K, respectively. Under the designed flight Mach number, the air stream can achieve a speed as high as 3119 m/s and a dynamic pressure of 30,325 Pa. Considering the viscous effect on the development of the boundary layer, the air captured by the inward-turning inlet is determined to be 1.47 kg/s. The whole operation time of the JF-24 shock tunnel takes only about 16 ms; thereby, the scramjet wall can be assumed to maintain at room temperature during the test. Ethylene is injected sonically through the 1.2-mm-diam portholes with a total temperature of 300 K (temperature in the test room). The fuel mass flow rates corresponding to fuel-lean (global equivalence ratio $\Phi = 0.6$), stoichiometric ($\Phi = 1.0$), and fuel-rich ($\Phi = 1.4$) conditions were configured.

The whole test lasts for 16 ms, which is the maximum operation time of JF-24. The fuel injection starts at $t = 1$ ms, and the signals from the pressure transducers reach a steady plateau from $t = 4$ to 7 ms. The pressure averaged over the middle range from $t = 5$ to 6 ms is compared in this study. Three individual tests under the same configurations were conducted to check the repeatability of the results. Wall heat flux was not measured because the maximum heat flux in hypersonic combustion exceeds the measuring range of most commercial and in-house designed heat flux sensors [53].

As shown in Fig. 2a, the computational domain consists of the 5.61-m-long internal and 0.67-m-long external flow regions. To verify the grid convergence, five sets of meshes with cell numbers ranging from 79.31 million (referring to 79.31M), 105.40 million (referring to 105.40M), 147.20 million (referring to 147.20M), 249.28 million (referring to 249.28M), to 368.34 million (referring to 368.34M) are used. The unstructured mesh is constructed by using the tetrahedron cells for their flexibility in filling complex geometry. The mesh is adaptively refined around the fuel injectors with a minimum size of 0.1 mm and transited by a growth ratio of 1.03. The different sizes of meshes are generated by adjusting the mean cell size in the internal domain away from the wall. The boundary layer is meshed by 15 inflation layers with a total thickness of 1 mm, and the first near-wall layer has a dimensionless wall distance of $y^+ < 1$. Mesh quantity analysis shows that the average skewness is 0.19 with a standard deviation of 0.11, and the average orthogonal quality is 0.81 with a standard deviation of 0.1.

Fixed pressure, temperature, velocity, and mixture compositions, as listed in Table 1, are specified for the freestream and the fuel inlets. Assuming that the air freestream is initially in thermal equilibrium, its translational and vibrational temperatures are set to the equilibrium value. A Reynolds-averaged Navier–Stokes (RANS)-type turbulent inlet boundary condition is specified on the inlets, and a nominal turbulence viscosity is specified as $\nu_t/\nu = 1$. The wall turbulence effect is modeled by using a wall function that specifies the velocity profile in the laminar, buffer, and logarithmic subregions according to Spalding's law [54,55]. The engine and pylon walls were given a nonslip, isothermal boundary condition with a fixed wall temperature of 300 K. The nozzle exit is configured as a mixed boundary condition, with the zero-gradient boundary condition for the outflow and the fixed freestream flow condition corresponding to the Mach-10 and 37-km-altitude atmosphere, i.e., pure air with 433 Pa and 242 K, for the case of return flow.

B. Governing Equations

The unsteady and 3-D Favre-averaged compressible reactive Navier–Stokes equations (rNSE) are solved for a set of conservative variables ($\bar{\rho}$, $\tilde{u}_i$, H_t, $\tilde{\xi}$),

$$\frac{\partial \bar{\rho}}{\partial t} + \frac{\partial \bar{\rho}\tilde{u}_j}{\partial x_j} = 0 \tag{1}$$

$$\frac{\partial \bar{\rho}\tilde{u}_i}{\partial t} + \frac{\partial \bar{\rho}\tilde{u}_j\tilde{u}_i}{\partial x_j} + \frac{\partial \bar{p}}{\partial x_i} - \frac{\partial \tilde{\tau}_{ij}}{\partial x_j} = -\frac{\partial \tau_{ij}}{\partial x_j} \tag{2}$$

$$\frac{\partial \bar{\rho}\tilde{H}_t}{\partial t} + \frac{\partial \bar{\rho}\tilde{u}_j\tilde{H}_t}{\partial x_j} - \frac{\partial}{\partial x_j}\left(\bar{\rho}D_T\frac{\partial \tilde{H}_t}{\partial x_j} + \sum_{\alpha=1}^{L}\bar{\rho}D_\alpha\frac{\partial \tilde{Y}_\alpha}{\partial x_j}\tilde{H}_\alpha\right) - \frac{\partial \bar{p}}{\partial t} - \frac{\partial \tilde{u}_j\tilde{\tau}_{ij}}{\partial x_j} = -\frac{\partial \Psi_{T,j}}{\partial x_j} \tag{3}$$

$$\frac{\partial \bar{\rho}\tilde{\xi}}{\partial t} + \frac{\partial \bar{\rho}\tilde{u}_j\tilde{\xi}}{\partial x_j} - \frac{\partial}{\partial x_j}\left(\bar{\rho}D_\alpha\frac{\partial \tilde{\xi}}{\partial x_j}\right) = -\frac{\partial \Psi_{\xi,j}}{\partial x_j} \tag{4}$$

$$\frac{\partial \bar{\rho}\widetilde{\xi''^2}}{\partial t} + \frac{\partial \bar{\rho}\tilde{\boldsymbol{u}}_j\widetilde{\xi''^2}}{\partial \boldsymbol{x}_j} - \frac{\partial}{\partial \boldsymbol{x}_j}\left(\bar{\rho}D_\xi\frac{\partial \widetilde{\xi''^2}}{\partial \boldsymbol{x}_j}\right) = C_g\bar{\rho}D_\xi\left(\frac{\partial \tilde{\xi}}{\partial \boldsymbol{x}_j}\right)^2 - C_d\frac{2D_\xi}{\Delta^2}\widetilde{\xi''^2} \tag{5}$$

$$\rho_\eta\frac{\partial Q_\alpha}{\partial t} + \langle\rho\boldsymbol{U}|\eta\rangle_{\text{zone}}\cdot\nabla Q_\alpha - \left\langle\rho D\nabla\xi\cdot\nabla\left(\frac{\partial Q_\alpha}{\partial \eta}\right)\middle|\eta\right\rangle_{\text{zone}} - \langle\nabla\cdot(\rho D\nabla Q_\alpha)|\eta\rangle_{\text{zone}} = \rho_\eta\frac{D_\alpha}{D_\xi}\langle\chi|\eta\rangle_{\text{zone}}\frac{\partial^2 Q_\alpha}{\partial \eta^2} + \rho_\eta\left(\frac{D_\alpha}{D_\xi} - 1\right)M_\eta\frac{\partial Q_\alpha}{\partial \eta} + \rho_\eta\langle W_\alpha|\eta\rangle \tag{6}$$

$$\bar{p} = \bar{\rho}R\widetilde{T} = \bar{\rho}\left(R_u\left(\sum_{\alpha=1}^{L}Y_\alpha/W_{m,\alpha}\right)\right)\widetilde{T} \tag{7}$$

Downloaded by "Chinese Academy of Sciences (CAS), Institute of Mechanics" on April 11, 2024 | http://arc.aiaa.org | DOI: 10.2514/1.B39007

$$\widetilde{H}_t = \widetilde{H} + \frac{1}{2}\tilde{u}_i\tilde{u}_i = \widetilde{H}^0 + \int_0^T C_p\,\mathrm{d}T + \frac{1}{2}\tilde{u}_i\tilde{u}_i \tag{8}$$

Here the bar $(-)$ and the tilde $(\tilde{})$ represent averaged and Favre-averaged quantities, respectively. The energy equation can be expressed differently in terms of total enthalpy, sensible enthalpy, total internal energy, or sensible internal energy. Internal energy is usually selected for nonreacting flows, and enthalpy is preferable for reacting systems because most of the chemical energies are expressed in enthalpy forms [56–62]. To conserve the energy in high-Mach flows, the energy equation in terms of total enthalpy is adopted since it implicitly conserves the kinetic energy related to flow speed and the thermal energy related to temperature. Equation (6) is solved in the four-dimensional (4-D) space, i.e., 3-D spatial space plus one-dimensional (1-D) mixture fraction space, for each species to obtain the conditional species mass fraction Q_α. The Favre-mean mass fraction $\tilde{Y}_\alpha$ of species α is integrated from the conditional values Q_α with the weight of an assumed probability density function (PDF) $P(\eta)$. And $P(\eta)$ is given as a β-function of the mean mixture fraction $\tilde{\xi}$ and its variance $\tilde{\xi''^2}$, which are solved from Eqs. (4) and (5). The mean temperature is then reversely calculated from the mean enthalpy given the species composition $\tilde{T} = f(\tilde{H}, \tilde{Y}_\alpha)$ to account for the compressibility effect in supersonic flows [63,64]. Figure 3 shows the flowchart of the solving process of flow and combustion.

According to Stokes's hypothesis, which ignores the bulk viscosity, the shear-stress tensor for a Newtonian fluid is calculated as

$$\tilde{\tau}_{ij} = \bar{\rho}\nu(\widetilde{T})\left(2\widetilde{S}_{ij} - \frac{2}{3}\delta_{ij}\widetilde{S}_{kk}\right) \tag{9}$$

where ν is a temperature-dependent kinetic viscosity, and the strain-rate tensor of the resolved scales is calculated as

$$\widetilde{S}_{ij} = \frac{1}{2}\left(\frac{\partial\tilde{u}_i}{\partial x_j} + \frac{\partial\tilde{u}_j}{\partial x_i}\right) \tag{10}$$

Accurate submodels for the SGS nonlinearities are generally lacking in the literature, and they are often ignored in most LES modelings.

The Reynolds stress τ_{ij} and turbulent fluxes $\Psi_{T,j}$ and $\Psi_{\alpha,j}$ in Eqs. (2–5) are unclosed and require specific modeling. The Reynolds stress is defined as $\tau_{ij} = \bar{\rho}(\widetilde{u_i u_j} - \tilde{u}_i\tilde{u}_j)$ and modeled by the Boussinesq eddy viscosity hypothesis, where the Reynolds stresses are proportional to $\tilde{S}_{ij}$,

$$\begin{aligned}\tau_{ij} &= \underbrace{\left(\tau_{ij} - \frac{1}{3}\delta_{ij}\tau_{kk}\right)}_{\text{deviatoric}} + \underbrace{\frac{1}{3}\delta_{ij}\tau_{kk}}_{\text{isotropic}} \\ &= -\bar{\rho}\nu_{sgs}\left(2\tilde{S}_{ij} - \frac{2}{3}\delta_{ij}\tilde{S}_{kk}\right) + \frac{2}{3}\delta_{ij}k_{sgs}\end{aligned} \tag{11}$$

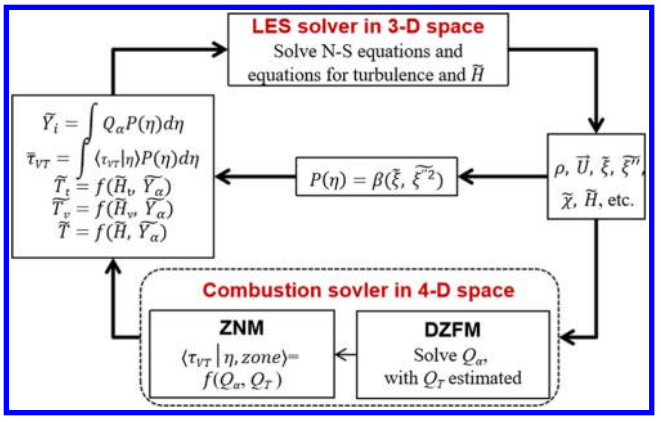

Fig. 3 Flowchart of the solving process of flow and combustion.

Here ν_{sgs} is the eddy viscosity given by $\nu_{sgs} = \tilde{\nu}f_{v1}$, and k_{sgs} is the unresolved subgrid-scale (SGS) kinetic energy that is determined reversely from ν_{sgs} as $k_{\text{sgs}} = [\nu_{sgs}/(C_k\Delta))]^2$. The turbulent viscosity is given by improved delayed detached eddy simulation (IDDES) based on k-ω shear stress transport model [65]. In wall-resolved LES (WRLES), the total number of grid points (N) scales with the Reynolds number (Re) as $N \sim Re^{13/7}$ [66], where the near-quadratic Re dependence makes it prohibitive for realistic supersonic flow modeling [67]. Thereby, IDDES is specially designed to address high-Re wall-bounded flows, e.g., supersonic flow in this study, by alleviating the modeling cost in the boundary layer to be $N \sim Re^1$ [66]. In addition to lowering the modeling cost of the turbulent boundary layer, the prominent advantage of IDDES lies in the direct resolving of a major part of the unsteady turbulent motions in the core internal region. The transition from the RANS to LES modes is mainly controlled by the definition of length scale, which determines the production and destruction levels of turbulent viscosity. The RANS mode uses the length scale defined as the distance to the nearest wall (d), while the LES mode uses the local grid size scaled by an empirical constant of $C_{DES}\Delta$. A more complicated definition of length scale l_{IDDES} is used [65,68] in IDDES to avoid a premature switching from RANS to LES at the edge of the turbulent boundary layer.

The turbulent enthalpy flux term $\Psi_{T,j} = \bar{\rho}(\widetilde{u_j H_t} - \tilde{u}_j\widetilde{H}_t)$ is modeled by the gradient diffusion assumption with a linear eddy diffusivity as

$$\Psi_{T,j} = -2\bar{\rho}\frac{\nu_t}{Pr_t}\frac{\partial\tilde{H}_t}{\partial x_j} \tag{12}$$

where Pr_t is the turbulent Prandtl number. The turbulent diffusion term for mixture faction $\Psi_{\xi,j} = \bar{\rho}(\widetilde{u_j\xi} - \tilde{u}_j\tilde{\xi})$ is similarly modeled as

$$\Psi_{\xi,j} = -2\bar{\rho}\frac{\nu_t}{Sc_t}\frac{\partial\tilde{\xi}}{\partial x_j} \tag{13}$$

where Sc_t is the turbulent Schmidt number. The choice of turbulent Prandtl and Schmidt numbers spans a large variation of 0.2–1.4 from case to case [69–74]. In this study, the optimal choice of unity Prandtl and Schmidt numbers is assumed (i.e., $Pr_t = 1$ and $Sc_t = 1$) for the internal flow region [69,75], while $Pr_t = 0.85$ is adopted for the turbulent boundary layer [76,77]. The unity Prandtl and Schmidt numbers have been embedded in the standard OpenFOAM code [78]. The choice of the turbulent Prandtl and Schmidt number may significantly influence the solution in RANS modelings; however, their influence is considered much smaller in highly resolved LES regions since SGS diffusivities are of orders of magnitude smaller [79]. A proper determination of turbulent Prandtl and Schmidt numbers in highly resolved LES for supersonic reacting flows merits future study to eliminate the modeling uncertainties further. Note that the laminar thermal and mass diffusivities are calculated directly based on the local thermodynamic states, i.e., pressure, temperature, and composition, instead of using the unity-Lewis number assumption to better account for the differential diffusion effect.

In resolving Eqs. (2–7), those subtle terms related to subgrid-scale nonlinearities and molecular partial diffusion are neglected. The nonlinearities in the diffusion terms in the momentum $(\bar{\tau}_{ij} - \tilde{\tau}_{ij})$, energy $(\bar{q}_j - \tilde{q}_j)$ and species equations $(\bar{J}_j - \tilde{J}_j)$ can be reasonably ignored based on the Direct Numerical Simulation study of a compressible mixing layer at Mach 0.2–0.6 [80]. SGS viscous dissipation $(\widetilde{u_j\tau_{ij}} - \tilde{u}_j\tilde{\tau}_{ij})$ is considered to be negligible in a priori test with DNS data for transitional boundary-layer flow at $Ma = 4.5$ [81]. The SGS fluctuations of the gas state in terms of unresolved temperature and species components introduced during the filtering process, $p_{sgs} = \bar{\rho}(\widetilde{RT} - \tilde{R}\tilde{T})$, may become significant in transcritical flows with substantial property gradients [82,83]; however, it is neglected in most existing modelings [84–86] because it is not expected to play a significant role in highly resolved LES simulations [87]. The thermal diffusion (Soret effect), pressure diffusion (baro-diffusion),

Downloaded by "Chinese Academy of Sciences (CAS), Institute of Mechanics" on April 11, 2024 | http://arc.aiaa.org | DOI: 10.2514/1.B39007

Downloaded by "Chinese Academy of Sciences (CAS), Institute of Mechanics" on April 11, 2024 | http://arc.aiaa.org | DOI: 10.2514/1.B39007

and mass-driven diffusion of heat (Dufour effect) become significant only when the participating species are of widely differing molecular weights [88–90], e.g., in the soot formation process with heavy soot particles involved, where lighter molecules are pushed away from heavier molecules in the direction of temperature, concentration, or pressure gradient. In addition, the diffusion time scale is much longer than the convection time scale in supersonic flows [35]. Therefore, those partial separation effects of the mixture due to molecule differences are not included in the current modeling.

C. Turbulent Combustion Model

The complete transport equations with differential diffusion and phase change for instantaneous mixture fraction ξ and mass fraction of individual species Y_α read as

$$\frac{\partial \rho}{\partial t} + \nabla \cdot (\rho \boldsymbol{U}) = \dot{m}_p \tag{14}$$

$$\frac{\partial \rho\xi}{\partial t} + \nabla \cdot (\rho \boldsymbol{U}\xi) = \left(\rho \frac{\partial \xi}{\partial t} + \rho \boldsymbol{U} \cdot \nabla \xi\right) + \xi\left(\frac{\partial \rho}{\partial t} + \nabla \cdot (\rho \boldsymbol{U})\right) - \nabla \cdot (\rho D_\xi \nabla \xi) = \dot{m}_p \xi_l \tag{15}$$

$$\frac{\partial \rho Y_\alpha}{\partial t} + \nabla \cdot (\rho \boldsymbol{U} Y_\alpha) = \left(\rho \frac{\partial Y_\alpha}{\partial t} + \rho \boldsymbol{U} \cdot \nabla Y_\alpha\right) + Y_\alpha\left(\frac{\partial \rho}{\partial t} + \nabla \cdot (\rho \boldsymbol{U})\right) - \nabla \cdot (\rho D_\alpha \nabla Y_\alpha) = \dot{m}_p Y_{l,\alpha} + \rho W_\alpha \tag{16}$$

The liquid mixture fraction is defined as $\xi_l = \sum Y_{l,\alpha}$, where species α belongs to the fuel species, and thus for pure liquid fuel droplet, $\xi_l = 1$.

To achieve high-efficiency yet high-fidelity modeling of high-Re turbulent reacting flow involving complex chemistry, dynamic zone flamelet model (DZFM) [10,91] is proposed based on the idea of dynamically dividing the computational domain into a finite number of zones and representing the local reacting status with an individual flamelet. Here, the terminology "dynamic" means that both the flamelet and its corresponding zone constantly evolve with the unsteady flowfield. DZFM introduces the concept of local conditional variable $Q_\alpha = \langle Y_\alpha | \xi(x,t) = \eta, x \in \text{zone}\rangle$, where η means the sampling variable in mixture fraction space, x represents the physical coordinate, and $x \in$ zone denotes that the conditional average is confined within the zone. Correspondingly, the instantaneous mass fraction is related to Q_α as

$$Y_\alpha(x,t) = Q_\alpha(\eta = \xi(x,t), x \in \text{zone}, t) + Y''_\alpha(x \in \text{zone}, t) \tag{17}$$

where Y''_α is the deviation of instantaneous value from the conditional average within the current zone, or more briefly, the conditional fluctuation. Note that the $\langle Y''_\alpha | \eta, x \in \text{zone}\rangle = 0$, and zone-averaged $\langle Y''_\alpha \rangle_{\text{zone}} = \int \langle Y''_\alpha | \eta, x \in \text{zone}\rangle P(\eta)\, \mathrm{d}\eta = 0$. $P(\eta)$ represents the PDF that describes the distribution of instantaneous ξ within the zone. In conditional-moment-based models, the key to valid the first-order closure assumption of nonlinear conditional chemical source terms [92] is reducing the fluctuations to a much low level ($Y'_\alpha \to 0$), which is difficult if the conditional mean is defined for the whole domain and can usually be achieved by introducing multiple conditioning [93–95]. For zone-based conditioning, a local statistical homogeneity of conditional means can be achieved by the combined use of two approaches, i.e., refining the zone division and adding more zone dividing indices, e.g., mixture fraction (ξ), Mach number (Ma), reaction progress variable (c), and streamwise distance (x) used in this study.

Differentiating Eq. (17) and substituting it into Eq. (16), then combining with Eqs. (14) and (15), one arrives at the following equation:

$$\rho \frac{\partial Q_\alpha}{\partial t} + \rho \boldsymbol{U} \cdot \nabla Q_\alpha + Y_\alpha \dot{m}_p - \dot{m}_p Y_{l,\alpha} - \rho D_\alpha (\nabla \xi)^2 \frac{\partial^2 Q_\alpha}{\partial \eta^2} + \frac{\partial Q_\alpha}{\partial \eta}\Bigg(\underbrace{\rho \frac{\partial \xi}{\partial t} + \rho \boldsymbol{U} \cdot \nabla \xi - \nabla \cdot (\rho D_\xi \nabla \xi)}_{\dot{m}_p \xi_l - \dot{m}_p \xi}\Bigg) + \left(1 - \frac{D_\alpha}{D_\xi}\right) \nabla \cdot (\rho D_\xi \nabla \xi) \frac{\partial Q_\alpha}{\partial \eta} + \left(\rho \frac{\partial Y''_\alpha}{\partial t} + \rho \boldsymbol{U} \cdot \nabla Y''_\alpha - \nabla \cdot (\rho D_\alpha \nabla Y''_\alpha)\right) - \rho D_\alpha \nabla \xi \cdot \nabla\left(\frac{\partial Q_\alpha}{\partial \eta}\right) - \rho D_\alpha \nabla^2 Q_\alpha = \rho W_\alpha \tag{18}$$

Taking conditional average on Eq. (18) with the following conditions: 1) $\xi(x,t) = \eta$, and 2) sampling within the local zone $x \in$ zone, the representative flamelet equation in terms of conditional species Q_α can be written as

$$\rho_\eta \frac{\partial Q_\alpha}{\partial t} + \langle \rho \boldsymbol{U} | \eta \rangle_{\text{zone}} \cdot \nabla Q_\alpha + \underbrace{E_{\text{vap}}}_{\text{not used}} + E_{ZFM} = \rho_\eta \frac{D_\alpha}{D_\xi} \langle \chi | \eta \rangle_{\text{zone}} \frac{\partial^2 Q_\alpha}{\partial \eta^2} + \rho_\eta \left(\frac{D_\alpha}{D_\xi} - 1\right) M_\eta \frac{\partial Q_\alpha}{\partial \eta} + \rho_\eta \langle W_\alpha | \eta \rangle \tag{19}$$

with

$$E_{\text{vap}} = \langle \dot{m}_p \rangle_{\text{zone}} \left(Q_\alpha - Q_{l,\alpha} + \frac{\partial Q_\alpha}{\partial \eta}(\xi_l - \eta)\right) \tag{20}$$

$$E_{ZFM} = \Big\langle \underbrace{\rho \partial Y''_\alpha / \partial t + \rho \vec{U} \cdot \nabla Y''_\alpha - \nabla \cdot (\rho D_\alpha \nabla Y''_\alpha)}_{e_Y} \Big| \eta \Big\rangle_{\text{zone}} - \left\langle \rho D \nabla \xi \cdot \nabla\left(\frac{\partial Q_\alpha}{\partial \eta}\right) \Big| \eta \right\rangle_{\text{zone}} - \langle \nabla \cdot (\rho D \nabla Q_\alpha) \eta \rangle_{\text{zone}} \tag{21}$$

The conditional redistributing term e_Y in E_{ZFM} diminishes as the zone division is adaptive to mixture fraction. The second and third terms in E_{ZFM} characterize the diffusion between the flamelets in different zones and was often neglected for high-Reynolds turbulent flows [96]. However, they can become important for weakly and moderately turbulent flows, such as the subsonic flow regions in the domain, and thus were included in this modeling by using a statistical conditional averaging method [97], which is especially suitable for high-resolution LES data. As liquid condense fuels are frequently used in scramjets, Eqs. (14–21) derive the complete mathematical equations for modeling either single-phase or two-phase combustion. A subscript below the phase change term E_{vap} was added in Eq. (19) to classify that this term is not used in the current modeling but can potentially be used in future studies if a phase change is involved. The conditional fuel composition $Q_{l,\alpha} = \langle Y_{l,\alpha} | \eta \rangle_{\text{zone}}$ is calculated as the pure mixing state between the liquid fuel composition $Y_{l,\alpha}$ and the oxidizer stream composition Y^0_α. For multicomponent liquid fuel, the evaporation heterogeneity among the liquid components can change the liquid composition from location to location, and by definition, the conditional fuel composition $Q_{l,\alpha}$ varies from zone to zone. Therefore, the zone should be dynamically updated to ensure local homogeneity in liquid fuel composition. Such a treatment of dynamic-zone-based conditional modeling makes the model applicable to spray combustion with heterogeneous evaporation behavior, which is the case in most engine combustors, while avoiding the introduction of complex double conditioning [96,98]. Another issue that should be paid special attention to in the scramjet design when using liquid fuels is that the heat absorption due to vaporization may cause observable low-temperature regions immediately behind the fuel injectors, which will anchor the flame at a more downstream location. In this study, because gaseous ethylene is used and no liquid phase was involved, the zone-average phase change rate $\langle \dot{m}_p \rangle_{\text{zone}}$ and the phase change term E_{vap} are excluded from Eq. (19) as Eq. (6). The zone-based conditional diffusion $M_\eta = \langle \nabla \cdot (D_\xi \nabla \xi) | \eta \rangle_{\text{zone}}$, the zone-based conditional scalar dissipation rate $\langle \chi | \eta \rangle_{\text{zone}}$, and the zone-based

Downloaded by "Chinese Academy of Sciences (CAS), Institute of Mechanics" on April 11, 2024 | http://arc.aiaa.org | DOI: 10.2514/1.B39007

conditional temperature $Q_T = \langle T|\eta\rangle_{\text{zone}}$ are all estimated by the statistical conditional averaging method [97] within each zone.

The combustion chemistry of ethylene burning with air is described by the skeletal kinetic mechanism consisting of 66 irreversible reactions between 23 species, which was developed by Zettervall et al. [99] and referred to as the Z66 mechanism. The mechanism has been extensively validated for combustion characteristics related to ignition and flame propagation over a wide range of pressure, temperature, and equivalence ratios. The mechanism accuracy is overall satisfactory over the range of conditions relevant to ramjet and scramjet applications.

The first-order closure, which considered that the conditional fluctuations are of smaller order than the conditional means ($Y''_\alpha < Q_\alpha$) and also smaller than the unconditional fluctuations ($Y''_\alpha < Y'_\alpha$) [92,100], is used to calculate the zone-based conditional chemical source terms:

$$\langle W_\alpha|\eta\rangle_{\text{zone}} \approx W_\alpha(Q_\alpha, Q_T) \tag{22}$$

D. Nonequilibrium Effects

The thermal nonequilibrium was accounted for by the two-temperature model [23,101], which subgroups the translational and rotational temperatures into a single transrotational temperature denoted by T_t, and the electron, electronic energy, and vibrational energy modes into a single vibrational–electronic temperature denoted by T_v. Such a two-temperature model was frequently employed in modeling supersonic combustion inside scramjets [29,31,102] and hypersonic reacting flow around aerobraking vehicles [24,28,30]. The underlying assumptions of such a lumped temperature treatment are that 1) the translational and rotational temperatures can achieve equilibrium with each other within a small number of particle collisions, and similarly, 2) electron and electronic energy modes can equilibrate with the vibrational energy mode at an almost infinitely fast speed based on the direct simulation Monte Carlo (DSMC) analysis [101,103]. However, the number of collisions needed to bring rotational temperature to the translational temperature increases with temperature, and at temperatures above 10,000 K, the rotational temperature must be recognized as a separate temperature, which leads to a three-temperature model [101]. The maximum temperature in most engine combustors will not exceed 5000 K; thus, the two-temperature model will suffice. In addition, this study does not take into account of the multiple vibrational modes, which assumes vibrational–electronic temperature for each vibrationally excited species and is thus extremely costly in both computational time and memory requirement for combustion modelings that usually involve plenty of species. The influence of multiple-vibrational model will be investigated in a future study.

A zonal nonequilibrium model (ZNM) is developed to account for the turbulence effect and improve computational efficiency. In ZNM, the flow domain is divided into different zones by using the indices of pressure, temperature, and mixture fraction, on the premise that the cells in each zone have a similar vibrational-translational relaxation time. Then for each zone, the conditional relaxation time is expressed in terms of conditional means following the semi-empirical correlation proposed by Millikan and White [104] (τ_{VT}^{MW}) and further corrected by Park [101] (τ_{VT}^{P}):

$$\langle \tau_{VT}|\eta, \text{zone}\rangle = \frac{101325}{\langle p\rangle_{\text{zone}}}\exp(A_s(\langle T_t|\eta\rangle^{-1/3} - B_s) - 18.42) + \left(\sqrt{\frac{8R\langle T_t|\eta\rangle}{\pi}}\cdot\sigma\left(\frac{5000}{\langle T_t|\eta\rangle}\right)^2\cdot n\right)^{-1} \tag{23}$$

The mean relaxation time is integrated by a β-function PDF:

$$\tau_{VT} = \int \langle \tau_{VT}|\eta, \text{zone}\rangle P(\eta)\,\mathrm{d}\eta \tag{24}$$

The energy exchange between the transrotational and the vibrational–electronic energy modes, abbreviated as V-T energy exchange, is calculated by the Landau–Teller equation [105]:

$$Q_{VT} = \sum_\alpha \left(\rho\frac{H_{tr} - H_{\text{vel}}}{\tau_{VT}}\right) \tag{25}$$

where H_{tr} and H_{vel} are the transrotational and vibrational–electron–electronic energies, respectively.

The nonequilibrium chemistry describing the air dissociation is simulated by Park's five-species mechanism [24,27,106], with three dissociation reactions for diatomic species and two exchange reactions involving NO. The five-species air dissociation chemistry is added to the combustion mechanism that describes the oxidization of the fuel. In this study, the chemistry–vibration coupling for the three main initiation reactions is calculated by Park's model optimized by the quasi-classical trajectory (QCT) method [107], while all the other reactions are treated by the coupled vibration–chemistry–vibration (CVCV) model [25,108]. In Park's model, the reaction rates are described based on a modified temperature, which is a function of both the translational and vibrational temperatures.

$$k(T_t, T_v) = \phi(T_t, T_v)k_{\text{eq}}(T_t) \approx k_{\text{eq}}(T_{\text{eff}}) \tag{26}$$

$$T_{\text{eff}} = (T_t T_v^\zeta)^{1/(1+\zeta)} \tag{27}$$

The parameter ζ is set to 1 in Park's original model, assuming that T_t and T_v affect the reaction rate identically; ζ can be optimized with QCT calculations using ab-initio-derived potential energy surfaces [107]. Table 2 lists the optimized ζ for the main reactions and the root-mean-square (RMS) errors of the approximate efficiency function.

In the CVCV model, the thermal nonequilibrium reaction rates are corrected with the efficiency function $\phi(T_t, T_v)$

$$k(T_t, T_v) = \phi(T_t, T_v)k_{\text{eq}}(T_t) \tag{28}$$

Here the vibrational partition function is defined for a harmonic oscillator with the characteristic vibrational temperature θ_v truncated to a maximum energy E as

$$Q(T; E) = \frac{1 - e^{-E/RT}}{1 - e^{-\theta_v/T}} \tag{29}$$

Here, the efficiency function can be calculated as

$$\phi(T_t, T_v) = X_1\frac{X_2}{X_3} \tag{30}$$

where

$$X_1 = \frac{Q(T_t; E_d)}{Q(T_v; E_d)} \tag{31}$$

$$X_2 = e^{-\gamma E_a/RT}Q(T_\Gamma; \gamma E_a) + Q(T^0; E_d) - Q(T^0; \gamma E_a) \tag{32}$$

$$X_3 = e^{-\gamma E_a/RT}Q(-T_U; \gamma E_a) + Q(T^*; E_d) - Q(T^*; \gamma E_a) \tag{33}$$

Here E_a is the reaction activation energy and E_d is the dissociation energy of the polyatomic molecule; γ determines the fraction of vibrational energy needed to overcome the activation threshold and

Table 2 Fitted parameters for optimized Park's model and the RMS errors

	All T_v		$0.5T_t \le T_v \le 1.2T_t$	
Reaction	ζ	Error	ζ	Error
$H + O_2(T_v)$	0.307	0.058	0.162	0.012
$O + H_2(T_v)$	0.155	0.064	0.071	0.010
$OH + H_2(T_v)$	0.114	0.020	0.087	0.016
$OH(T_v) + H_2$	0.016	0.004	0.012	0.003

Downloaded by "Chinese Academy of Sciences (CAS), Institute of Mechanics" on April 11, 2024 | http://arc.aiaa.org | DOI: 10.2514/1.B39007

is set to 0.8. The pseudotemperatures T^0, T^*, T_Γ, and T_U are defined as follows:

$$T_U = \frac{E_d}{5R} \tag{34}$$

$$\frac{1}{T_\Gamma} = \frac{1}{T_v} - \frac{1}{T_t} - \frac{1}{T_U} \tag{35}$$

$$\frac{1}{T^0} = \frac{1}{T_v} - \frac{1}{T_U} \tag{36}$$

$$\frac{1}{T^*} = \frac{1}{T_t} - \frac{1}{T_U} \tag{37}$$

It should be noted that the CVCV model is suitable for reactions involving only one polyatomic reactant. The lowest characteristic vibrational temperature is used for the triatomic molecules with multiple vibrational modes.

The vibrational–electronic energy added or removed by chemical reactions is calculated as

$$Q_{CV} = \dot{\omega}(D' + e_{\text{el}}) \tag{38}$$

where e_{el} is the electronic energy and D' is the dissociation energy. A preferential model [109], which assumes that molecules are more likely to dissociate at higher vibrational energy states, is used to calculate D' as the dissociation potential scaled by a constant fraction of around 0.3.

E. Computational Configurations

The computation is conducted by a compressible combustion solver Amber [35,91,110–115] developed in the framework of OpenFOAM V2112 [116]. The main design principle of Amber is zone-based decoupling modeling of turbulent flow, chemical kinetics, and physical properties [10]. The chemistry and property are resolved in the local conditional space belonging to each zone and then fed back to the flow solver through PDF integrations. In the premise of satisfying local statistical homogeneity, i.e., no statistical dependence of the local states on space other than the conditioning variable(s) [117], the dynamic adaptive zone division enables a local flow–chemistry–property decoupling. The thermodynamic nonequilibrium effects are handled in the stage of property computation by the ZNM [10]. The chemistry solving in the conditional space can be further accelerated by ISAT and DAC [118].

The inviscid flux is resolved by a low-Mach corrected hybrid KNP/central scheme [119–121], which combines the dissipative KNP scheme [122] with the nondissipative central scheme [123]. Face variables for constructing the convective fluxes are interpolated by a third-order low-dissipation scale-selective discretization scheme (SSD) [124]. The central discretization scheme with nonorthogonal correction is applied for the diffusion terms. The time step is advanced by the second-order Crank–Nicolson scheme [125].

The molecular viscosity is calculated by Blottner's viscosity model [126], and the thermal conductivity is given by Eucken's formula [127]. Specific heat and enthalpy are calculated by temperature-dependent curve-fit models [128]. The vibrational and electronic enthalpies are calculated based on their characteristic temperatures and the degeneracy degree of the electronic level [30]. The mass diffusivities of individual species are calculated using the chemical kinetics package CHEMKIN-II [129] based on the transport database containing the molecular parameters for each species, such as Lennard–Jones potential well depth, Lennard–Jones collision diameter, and dipole moment. The specific heat and enthalpy of the mixture are calculated by molar-fraction-weighted averaging. The mixture-averaged viscosity is calculated by the modified Wilke's mixing law [130,131]. The mixture-averaged thermal conductivity is calculated by the combination averaging formula [132]. To account for the differential diffusion effect, the mixture-averaged diffusion coefficient for each species is calculated by Bird's formula [130,133].

MPI parallel computations based on domain decomposition were performed in the national supercomputer center by the TianHe-HPC4 cluster, which is composed of Intel(R) Xeon(R) Gold 6240 CPUs with a base frequency of 2.6 GHz. All the computations were run parallel on 360 cores. The time step is limited by a maximum Courant number of 0.5 and a user-specified maximum time step of 5×10^{-8} s, roughly 1/10–1/20 of the chemical time scale. Considering the total length of the internal engine flow path (5.61 m) and the external flow domain (0.67 m), the flush through time (FTT) calculated based on the initial flow speed of the air freestream (3119 m/s) is 2 ms. The modeling case with 368.34 million cells takes $24 \times 24 \times 360$ CPU hours to ensure 3 FTTs for the data sampling and statistics. The computational time of the other cases roughly scales with the mesh size.

III. Results and Discussion

Figure 4a compares the predicted and measured wall pressure. The pressure profiles were similar for the nonequilibrium cases, and the mean errors relative to the result based on the finest mesh show a clear converging trend as the mesh is refined. The prediction by 147.20M mesh has a small relative error of less than 1%; thereby, the following analyses are all based on 147.20M mesh unless otherwise specified. In the analysis, the equilibrium case assumes thermal equilibrium and excludes the air dissociation chemistry, while the nonequilibrium case assumes thermal nonequilibrium and employs Z66 plus air dissociation chemistry that accounts for the influence of the vibrational energy mode. The prediction assuming equilibrium is overall higher than the nonequilibrium predictions. The agreement of the nonequilibrium prediction based on the 147.2M mesh with the experimental measurement is generally better, though with somewhat overprediction of the peak pressure around the fuel injectors and the cavity. The discrepancy is probably due to the differences between the direct-connect inflow and the inlet-compressed free flow. The shock-compressed inflow has experienced an extremely high temperature up to the stagnation temperature of 3843 K; thus,

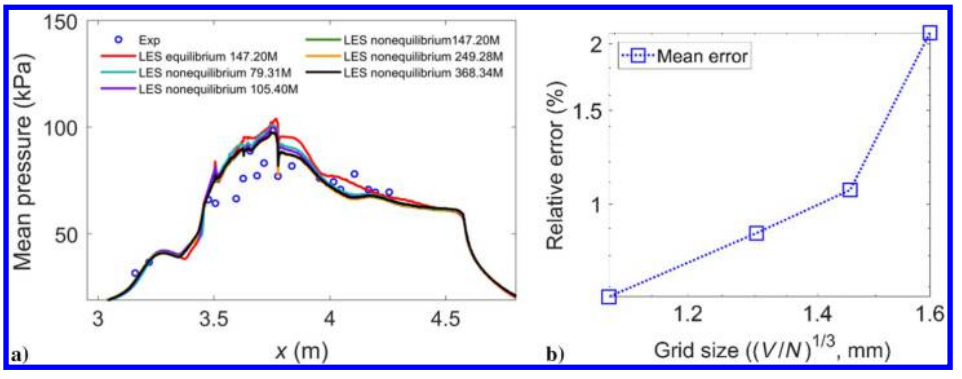

Fig. 4 a) Streamwise mean wall pressure under $\Phi = 0.6$; b) grid convergence analysis in log-log coordinate.

Downloaded by "Chinese Academy of Sciences (CAS), Institute of Mechanics" on April 11, 2024 | http://arc.aiaa.org | DOI: 10.2514/1.B39007

the air inflow can be considered fully dissociated. The subsequent acceleration by the Laval nozzle temporally reduces the flow temperature, but the molecule recombination may not be fully recovered, given the short flow residence time, whereas the modeling reproduced the actual flow status at the entrance of the isolator by including the inlet flow as well as part of the external flow, in which the air dissociation level gradually increases with the temperature rise under the inlet compression. Another factor that may affect is the difference in inflow turbulence level. As pointed out in [42], the strong shock wave/turbulent boundary-layer interaction at the throat of the Laval nozzle causes a thicker boundary layer and a negative effect on flow uniformity. Although the shock tube can reproduce a test gas with pressure, temperature, and Mach number similar to the actual flight test, the subtle effects of gas composition and turbulence intensity are more challenging to reproduce simultaneously. To achieve consistent data with the actual flight test, a full-component performance evaluation of the ensemble scramjet is required for both the experimental and numerical studies, implying that a larger-scale shock tube and more computational resources are needed.

Figure 5 compares the reacting flowfields under equilibrium and nonequilibrium. Under all the modeled conditions, there is flame propagation along the recirculation zone upstream of the injectors. The flame upstream propagation distance generally increases with the fuel equivalence ratio, while the propagation distance assuming equilibrium under the fuel-lean condition ($\Phi = 0.6$) is comparable to the nonequilibrium case with the highest equivalence ratio ($\Phi = 1.4$), suggesting that much more heat addition has been imposed into the supersonic flow if assuming equilibrium. The contours of $Ma = 1$ overlaid with the temperature field show that the upstream recirculation zone not only slows down a large portion of the flow to be subsonic but also enhances the mixing by entraining both the fuel and air. A ramjet mode rarely occurs in hypersonic combustors, as the thermal choking is difficult to be established as the freestream velocity increases. It is noticed that the upstream propagation only occurs before those pylon-based injectors. The changed incoming flow and boundary layer exert different impacts on the corresponding downstream injection: 1) the reduced local flow momentum flux or dynamic pressure facilitates the jet penetration of the injections from the pylon top, near which a thicker reaction layer was formed; 2) on the other hand, the jet penetration of the wall-injected jets has been significantly suppressed, and the flame is blown downstream and stabilized in the downstream cavity. Typically, the flame stabilization mode can be classified as the cavity mode, the jet-wake mode, and the oscillation mode [134]. The use of a pylon creates a new upstream recirculation mode, which can be considered a special type of jet-wake mode. The jet-wake mode is favorable because it usually implies better near-field combustion efficiency or, more pertinently, a shorter combustor length. As discussed in [135], the traditional flame-holding strategy of using a cavity is considered of less use for scramjets operating at high-Mach flight conditions. The current modeling shows that the sole use of a cavity is not enough, whereas a pylon should be used instead, or at least combinedly.

Generally, there are two effects induced by thermal nonequilibrium, i.e., the *nonequilibrium heating effect* and the *nonequilibrium cooling effect*.

1) Because the establishment of equilibrium inevitably has a certain delay, usually in the order of $10^{-5} - 10^{-2}$ s inside scramjets [10], the addition of kinetic energy to the transrotational energy mode due to flow compression and viscous heating will temporarily raise T_t

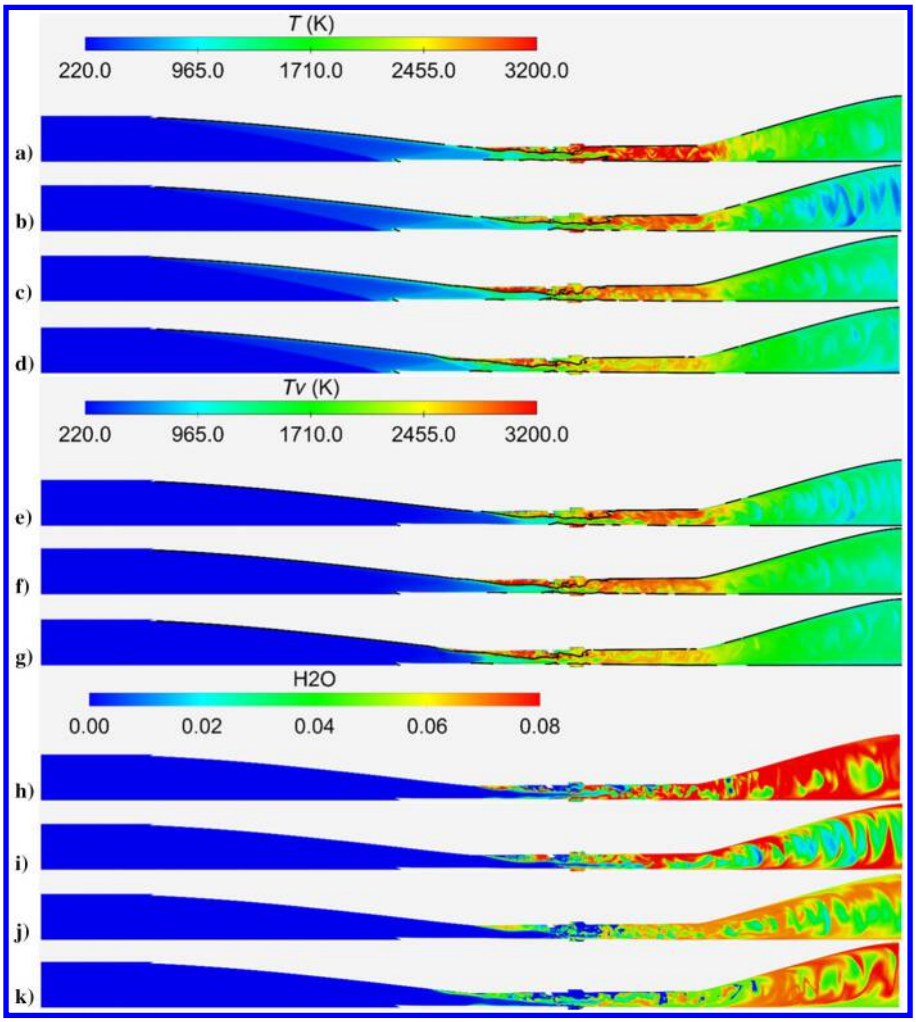

Fig. 5 a) T in the thermal equilibrium case under $\Phi = 0.6$; T_t in the nonequilibrium case under b) $\Phi = 0.6$, c) $\Phi = 1.0$, and d) $\Phi = 1.4$; T_v in the nonequilibrium case under e) $\Phi = 0.6$, f) $\Phi = 1.0$, and g) $\Phi = 1.4$; h) T in the thermal equilibrium case under $\Phi = 0.6$; mass fraction of H_2O in the nonequilibrium case under i) $\Phi = 0.6$, j) $\Phi = 1.0$, and k) $\Phi = 1.4$.

Downloaded by "Chinese Academy of Sciences (CAS), Institute of Mechanics" on April 11, 2024 | http://arc.aiaa.org | DOI: 10.2514/1.B39007

to above the equilibrium value T, exhibiting as *nonequilibrium heating effect*. The nonequilibrium heating effect increases T_t near the wall, causing an observable thickening of the boundary layer along the internal surface of the inward-turning inlet. The V-T energy exchange is negligible for $T_t < 800$ K; therefore, the cold internal regions of the inlet flow are visually similar for the equilibrium and nonequilibrium cases. Because the thickening of the boundary layer due to the nonequilibrium heating effect becomes prominent only after the inlet cowl, the air capturing rate is less affected, with a negligible discrepancy of around 0.3% for the equilibrium and nonequilibrium cases. In addition to thickening the boundary layer, the higher T_t in the boundary layer can also lead to an early ignition, as reported in [31]. However, due to the existence of the upstream recirculation zone, the early ignition cannot be distinguished from the premixing effect of the recirculation zone in the current modeling.

2) In contrast, the deduction of kinetic energy from the transrotational energy mode due to flow expansion will temporarily reduce T_t to below its equilibrium value T, exhibiting the *nonequilibrium cooling effect*. In the nozzle, excessive kinetic energy has been solely extracted from the transrotational mode, which was not compensated by the vibrational–electronic mode immediately. Such a nonequilibrium cooling effect results in a noticeable drop in T_t characterized by the cold streaks, which are more evident under $\Phi = 0.6$ due to insufficient heat addition and are barely observed when increasing the fuel supply. Since the kinetic energy is solely extracted from the transrotational energy, the flow expansion has no immediate influence on T_v. A new thermal equilibrium will be reached between T_t and T_v if given sufficient thermal relaxation time of the order of microseconds. The final product H_2O was richly produced in the nozzle for the equilibrium case, while much less under nonequilibrium, suggesting that the reactions there have been significantly weakened by the nonequilibrium cooling effect.

Note that the above observation is made for supersonic flows. For subsonic flows, the observation is reversed; i.e., the compression of a subsonic flow will lead to the *nonequilibrium cooling effect*, and the expansion of a subsonic flow will cause the *nonequilibrium heating effect.* A general rule of thumb is to see whether energy is added to or extracted from the transrotational energy mode. The nonequilibrium cooling effect has been prominently identified after the diverging part of the combustor in a previous study [10]. However, the early chain reactions initiated at the inlet fuel injection obscure the effects of thermal nonequilibrium and chemical nonequilibrium. The previously observed thinner boundary layer along the inlet cowl could be due to the degenerated reactivity under chemical nonequilibrium.

According to Eq. (23), aerodynamic compression is favorable for establishing thermal equilibrium, whereas aerodynamic expansion will further drive the flow away from thermal equilibrium. The compression, whether by isotropic wave or shock wave, firstly imposes part of kinetic energy into the translational–rotational energy, which then transfers to the vibrational energy to establish the thermal equilibrium. The high temperature and pressure behind the compression wave increase the collision frequency and facilitate the establishment of thermal equilibrium. The expansion causes the translational temperature to drop below the vibrational temperature [31], further increasing the thermal relaxation time and freezing the nonequilibrium status.

The flame temperature under nonequilibrium is both affected by the V-T energy exchange and the nonequilibrium chemistry, i.e., the thermal and chemical nonequilibrium effects. Inside the combustor, the equilibrium flame temperature is overall higher than the nonequilibrium one. The high-temperature region spreads more widely inside the combustor under the unity equivalence ratio, and the flame temperature decreases further under the fuel-rich condition due to the existence of unburnt high-heat-capacity fuel. The peak equilibrium temperature (T) is around 300 K higher than the peak transrotational temperature (T_t). Most of the flame temperature has reached 3500 K in the equilibrium case, while only 3200 K in the nonequilibrium case. In the current study, thermal equilibrium can be quickly established for the regions with a high flame temperature of over 2000 K, as confirmed by the observation that T_v is nearly identical with T_t inside the combustor. However, in the low-temperature inlet and isolator, the V-T energy exchange has been significantly delayed, and the resultant lower T_v weakens the initial reactions [29]. This indicates that although the nonequilibrium heating effect under combustion increases T_t and may promote an early ignition [31], the unsynchronous rise of T_v tends to suppress the combustion. The inclusion of nonequilibrium air chemistry induces additional air dissociation, which would further reduce the flame temperature.

The production of H_2O decreases with the increase of the global fuel equivalence ratio, which is in accordance with the reducing trend of the flame temperature. Such a tendency is somewhat contrary to the observation under moderate Mach conditions [110], where the combustion is usually enhanced with the increasing global fuel equivalence ratio. This suggests that the benefit of additional fuel was not fully released, primarily attributed to the poor mixing under higher equivalence ratios. Although it is claimed that reduced T_t has the advantage of strengthening turbulence and enhancing mixing [29], the prolonged reaction chains under chemical nonequilibrium increase the probability of incomplete combustion, i.e., the conversion process of reactants into the final products (i.e., CO_2 and H_2O) is more prone to be interrupted by stochastic convection. In this study, both the thermal nonequilibrium and chemical nonequilibrium were included in the modeling as what occurs in the actual flight test. However, to further distinguish their individual influences on the product production, numerical tests that enable each one solely will be conducted in a future study.

Figure 6 compares the evolution of flamelets from the upstream of the injectors to the nozzle exit with $\mathbf{\Phi} = 0.6$ under equilibrium and nonequilibrium. Although the first probed location $x = 3.69$ m is upstream of the first row of injectors ($x = 3.72$ m), the reaction in the upstream recirculation zone has already produced plenty of final products, i.e., CO_2 and H_2O. For the equilibrium case, the mass fraction of the final products quickly peaks at $x = 3.88$ m, then drops until reaching $x = 5.22$ m, after which the reacting statuses vary little and nearly converge to a single curve. The reaction is initially weak for the nonequilibrium case, and the concentrations of CO_2 and H_2O keep increasing until converging at around $x = 5.22$ m. The convergence of the reacting statuses indicates that the combustion reactions have reached a relatively stable status. In most of the flamelets, the final products in the mixture fraction space are more abundant in the equilibrium case, indicating a more complete burning. Therefore higher combustion efficiency of the short period from $x = 3.8$ to 5 m under nonequilibrium can only be attributed to the good mixing. Besides those coagulated flamelets, lean-shifting in the peaks of CO_2 and H_2O profiles away from the theoretical stoichiometric mixture fraction $\xi_{st} = 0.06355$ was observed. The off-stoichiometric phenomenon is partially because the chemistry has not reached equilibrium immediately downstream of the injectors and is also contributed by the differential diffusion effect. Due to the short flow residence time and the quick dispersion in supersonic flows, the actual fuel burnt is the small hydrocarbons and hydrogen pyrolyzed from ethylene. The high diffusivity of hydrogen over hydrocarbons makes it transfer faster and, accordingly, reduces the local stoichiometric mixture fraction. For slow chemistry in high-speed flows, those pyrolyzed intermediates determine the basic combustion properties rather than the original fuel directly. After incorporating the nonequilibrium air dissociation reactions, the peak concentrations of the O atom rise more than double compared with the equilibrium case. In the equilibrium case, the O can only be produced with the aid of hydrocarbon- or H-contained radicals. The O atom acts as an intermediate species and is quickly consumed in the main reaction region in the equilibrium case before $x = 5.03$ m, during which stages no obvious peaks can be observed while more O atoms remain in the downstream postcombustion region. Because an alternative path of direct oxygen dissociation is available for the O formation in the nonequilibrium case, O atoms are much more abundant during the main reaction stages and maintain nearly the same level as the equilibrium case in the postcombustion region after $x = 5.03$ m. The oscillations in the O profiles indicate that the reactions are more heterogeneous in the nonequilibrium case due to the complexity of nonequilibrium chemistry and the wide distribution of colder streaks inside the combustor. NO is massively produced under the oxygen-rich condition with the presence of a high temperature above 1800 K [136]. In this study, the reactions between N_2 and the hydrocarbon radicals

Downloaded by "Chinese Academy of Sciences (CAS), Institute of Mechanics" on April 11, 2024 | http://arc.aiaa.org | DOI: 10.2514/1.B39007

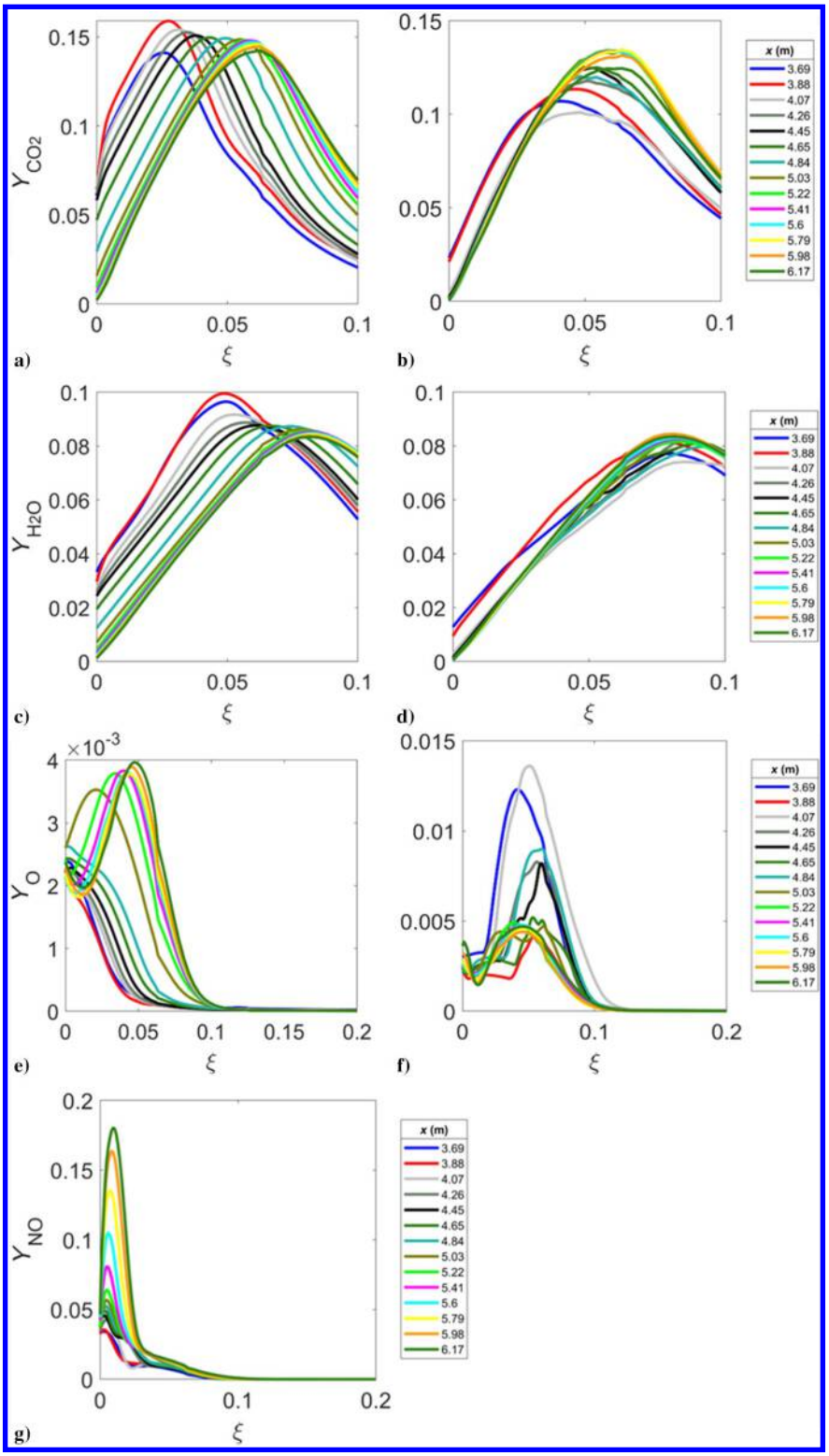

Fig. 6 Evolution of flamelets probed at locations from $x = 3.69$ to 6.17 m; mass fractions of a) CO_2, c) H_2O, and e) O atom under equilibrium; mass fractions of b) CO_2, d) H_2O, f) O atom, and g) NO radical under nonequilibrium.

are not included; thus, there is no NO formation in the colder part of the flame through the so-called prompt NO mechanism [136]. Since the air-dissociation reactions have not been included in the Z66 combustion mechanism [99], NO is not present in the equilibrium case. The comparable concentration of NO with the final products of H_2O and CO_2 implies substantial endothermic dissociation reactions, which significantly bring down the flame temperature, as compared in Figs. 5a and 5b. From Fig. 6g, NO is mainly formed in the fuel-lean side, or more precisely, mainly below $\xi < 0.05$; thus, the influence of nonequilibrium air chemistry should only cause a direct impact in the fuel-lean regions, e.g., the postflame region and the nozzle flow region. In the upstream recirculation zone, where the flame is partially premixed, the diffusion of fuel into the small ξ space bins implies that the air can be polluted by the small hydrocarbons and hydrogen radicals cracked from the fuel. The current study employs an extrapolation boundary condition in the mixture fraction space to better account for this effect.

Figure 7 compares the reaction paths under equilibrium and nonequilibrium to reveal the influence of chemical nonequilibrium. The chemical statuses are probed at three typical locations corresponding

Downloaded by "Chinese Academy of Sciences (CAS), Institute of Mechanics" on April 11, 2024 | http://arc.aiaa.org | DOI: 10.2514/1.B39007

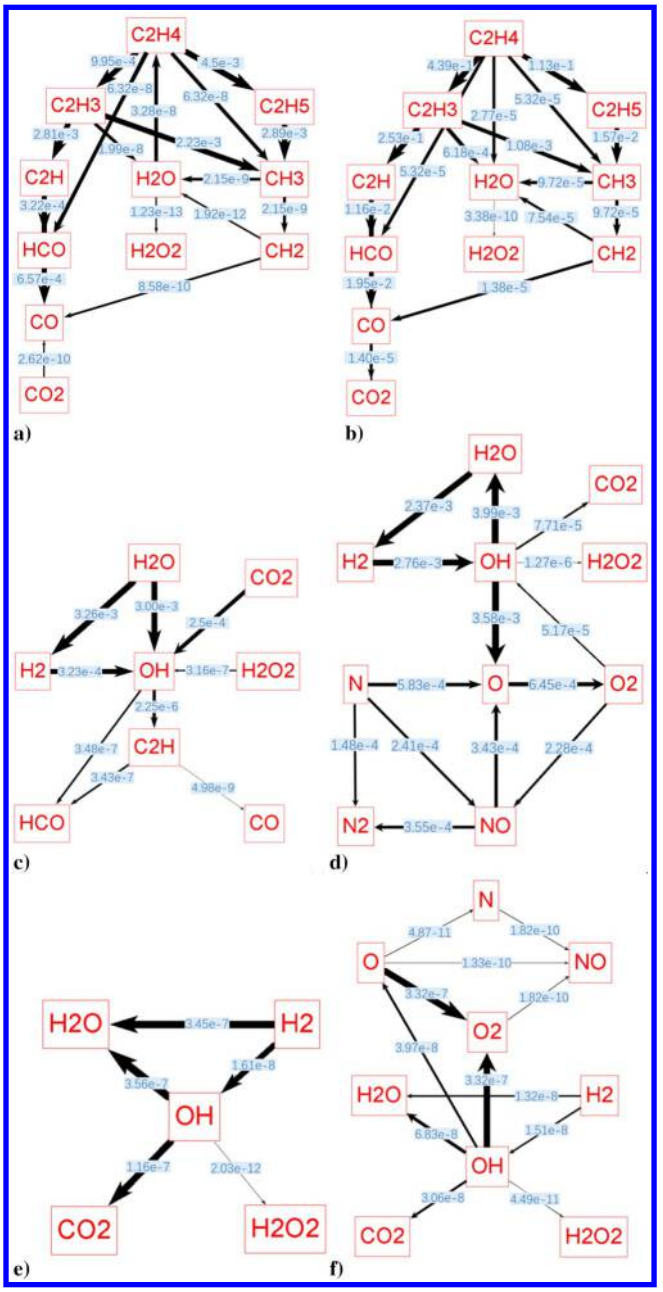

Fig. 7 Variation of reaction paths probed at an fixed off-wall distance of 3.26 cm and streamwise locations with $x = 3.72$ m (a, b), $x = 4.68$ m (c, d), and $x = 6.28$ m (e, f); reaction path fluxes are labeled by ROP with the unit of mol/(cm^3 s).

to the main reaction region, the postflame region, and the nozzle exhaust flow, respectively. The rate of production (ROP) is calculated directly for the local reacting statuses based on the Arrhenius formula with equilibrium temperature and the CVCV model with nonequilibrium temperatures. In the CVCV model, the reaction rate is weakened by reducing the efficiency function to $\phi < 1$ when $T_v < T_t$, and enhanced by raising the efficiency function to $\phi > 1$ when $T_v > T_t$ [107]. However, the base reaction rate is still determined by T_t, and the influence of vibrational nonequilibrium varies for different reactions and different reactant compositions. The reaction paths in Figs. 7a and 7b are generally similar at the first probing location close to the injectors, where the fuel is rich and complete reaction paths proceed to the final products. One of the major differences in the path structure is that the pyrolysis reaction from C_2H_4 to H_2O, i.e., $C_2H_4 + OH = C_2H_3 + H_2O$, has been reversed in the equilibrium case due to the absence of OH radicals. OH further helps the pyrolysis of C_2H_3 to C_2H_2 and, subsequently, C_2H. However, the role of OH in promoting pyrolysis is still trivial compared with the direct thermal cracking from C_2H4 to C_2H_3 and C_2H, i.e., $C_2H_4 \Rightarrow C_2H_3 + H$ and $C_2H_3 \Rightarrow C_2H + H_2$. Due also to the absence of OH, the conversion from CO to CO_2 was hindered, as the chain termination step $CO + OH \Rightarrow CO_2 + H$ is rate-limited by the concentration of OH. The OH formation through the chain reactions $O + H_2 \Rightarrow H + OH$ and $O + H_2O \Rightarrow OH + OH$ significantly relies on the O atom produced through the air dissociation. Although dissociated in a small quantity of 2×10^{-5} in mass fraction, the O atom considerably alters the downstream fuel-pyrolysis and CO-oxidation paths. As the indicator of combustion efficiency, H_2O was formed mainly through the dehydrogenation of hydrocarbons (e.g., C_2H_3, C_2H, CH_3) or hydrogen with OH, whose abundance in the nonequilibrium case raises the combustion efficiency over that of the equilibrium case temporarily from $x = 3.8$ to 5 m. There is a competition between the reaction paths of C_2H_4, one leading to C_2H_3 and one leading back to C_2H_5. The former is realized mainly through unimolecular thermal decomposition and fractionally through the dehydrogenation reaction with CH_3. The produced H atoms can be recombined into H_2, as elaborated in [137], or acts as an active H-abstractor from other alkyl or alkenyl radicals [138]. The latter's ratio in the total C_2H_4 consumption is 82% in the equilibrium case, while it reduces to 20% in the nonequilibrium case. This is mainly because the higher jet penetration depth under a more decelerated crossflow in the equilibrium case causes a lower near-field temperature, which significantly suppresses the thermal decomposition of C_2H_4. The product C_2H_5 of the latter reaction path is metastable and will be subsequently converted to CH_3 when attacked by H atoms. Figures 7c and 7d are probed at the joint point between the combustor and nozzle sections, where the fuel has been mostly consumed, and weaker reactions remain in the form of product dissociations, together with air dissociation when in the nonequilibrium case. The major difference between the two reaction paths is the additional nonequilibrium air dissociation reactions connected by OH. Due to the good mixing and higher combustion efficiency before the second probed location, nearly all the fuel has been converted into various oxides, e.g., CO, CO_2, and H_2O; therefore, there are no hydrocarbon-related reactions in the reaction path of the nonequilibrium case. CO is considered the primary product of hydrocarbon oxidation, and the conversion from CO to CO_2 is usually rate-limiting. A general rule of thumb is that the main oxidization reaction path of CO is through OH when the mass fraction of H_2O or H_2 is larger than 1% [137], which is satisfied in the current postflame regions. With rich OH in the nonequilibrium case, the conversion from CO to CO_2 has reached relatively stable, as confirmed by the weak net reaction path flux from CO (+OH) to CO_2. For the same reason of OH depletion, the conversion from OH to CO_2 has been reverted in the equilibrium case. A minimal amount of hydrocarbon remainings continue to react with OH, producing CH_2, HCO, and CO. It seems that for small alkyl radicals (e.g., C_2H_2, C_2H), the OH and O thermal decomposition dominates over those direct cracking reactions and the decomposition reactions by H-attacking at the first probing location [137]. Similarly, the reaction path probed near the nozzle exit in the nonequilibrium has additional air dissociation reactions connected by OH. With the reduction of temperature from above 2800 K at the second probing location to below 1000 K at the third probing location, the dissociation of N_2 becomes unimportant since breaking the tight N_2 bond is only favored under a high temperature above 1800 K. Under the lower temperature inside the nozzle, O and OH tend to recombine into O_2, while N and O will recombine into NO. Overall, the chemical nonequilibrium exerts more impact in the fuel-lean postflame regions, where the product dissociation has comparable path fluxes with the air dissociation. In the fuel-rich regions, the air dissociation reactions are much weaker than the intense combustion reactions, and the thermal nonequilibrium should take more effect through nonequilibrium heating/cooling as well as mixing enhancement. In the fuel-lean regions, the chemical nonequilibrium affects the combustion mainly through the key intermediate OH, and it seems that the air dissociation competes for OH with the product dissociation.

Figure 8 shows the quasi-one-dimensional performance analyses along the streamwise direction. The mixing starts early before the injectors, evidencing the role of the upstream recirculation zone as an

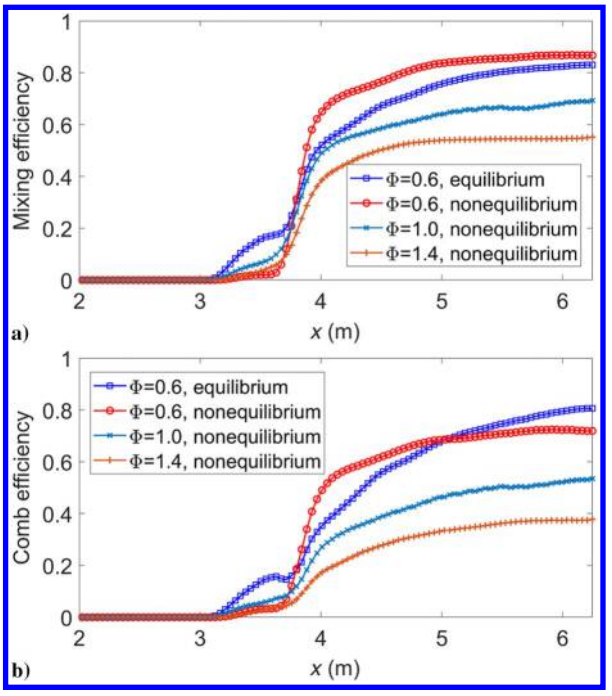

Fig. 8 Quasi-one-dimensional performance indices in the streamwise direction: a) mixing efficiency, and b) combustion efficiency.

efficient premixer. Although the recirculation zone propagates slightly more upstream under a higher $\boldsymbol{\Phi}$ in Fig. 5, the effective mixing starts roughly from the same location. In the upstream recirculation stage, the equilibrium mixing efficiency overwhelms those nonequilibrium values. For the nonequilibrium cases, the recirculation mixing under unity $\boldsymbol{\Phi}$ is better than both the fuel-lean and fuel-rich cases. Between the injectors and the cavity, the nonequilibrium mixing with $\boldsymbol{\Phi} = 0.6$ quickly strengthens and surpasses its equilibrium counterpart. After the cavity, the equilibrium mixing gains a higher rise rate to approach but is always beneath the nonequilibrium one throughout the nozzle. This can be explained by the reduced viscosity and strengthened flow turbulence under lower T_t [29]. In supersonic flows, the dilatational effect is dominant in vortex generation [35], while vortex stretching becomes weak because the vorticity and the velocity vectors are nearly aligned in the internal flow far from shocks and walls [139]. In the equilibrium case, the higher temperature near the cavity suppresses the vorticity generation by the dilatational effect [139] and consequently suppresses the mixing. The final mixing efficiencies under $\boldsymbol{\Phi} = 0.6$ are 86.7 and 83.0% for the equilibrium and nonequilibrium cases, respectively. Under nonequilibrium, the final mixing efficiency further decreases to 69.2 and 55.2% as the global equivalence ratio rises to 1.0 and 1.4. As seen, adequate mixing becomes a more urgent problem for hypersonic combustion, where the nominal flow residence time for combustion decreases to even below 1 ms under a hypersonic entrance flow speed [2].

With higher mixing efficiency, the final combustion efficiency of 72.5% under nonequilibrium is still lower than the 80.6% in the equilibrium case. This indicates that both the additional air dissociations and the chemistry–vibration coupling arising from chemical nonequilibrium make it harder to add heat into the high-enthalpy hypersonic flow to achieve a high specific impulse [11]. Due to the premixing role of the upstream recirculation zone, the combustion efficiency has risen considerably before the injectors, especially for the equilibrium case. For the equilibrium case, the combustion efficiency drops slightly near the injectors with the enrichment of unburnt fresh fuel. Whereas no observable drop exists in the mixing efficiency, suggesting that the mixing by intense near-field momentum exchange is more effective than the large-scale upstream recirculation. For the nonequilibrium case, the combustion efficiency has a sharper rise between the injectors and the cavity, where the heat addition from combustion expands the subsonic region considerably. After the cavity, combustion efficiency under nonequilibrium ascends more gently and is surpassed again by the one under equilibrium at the joint point between the combustor section and the nozzle section. The gradually weakened combustion after the cavity could be due to the incorporation of nonequilibrium air chemistry that produces dissociated radicals. The recombination of radicals was further frozen by the nonequilibrium cooling effect, which is the primary reason for the receding of reactivity in the divergent nozzle. The combustion efficiency then decreases to 53.5 and 37.8% as the global fuel equivalence ratio increases from 0.6 to 1.0 and 1.4. The significant discrepancies of over 10% between the combustion efficiency and the mixing efficiency imply that the combustion is partially controlled by chemistry for current hydrocarbon-fueled hypersonic combustion, where the reaction chains are usually much longer than in hydrogen combustion and the time scale of chemistry is comparable or even larger than with the flow residence time. Compared with hydrogen-fueled hypersonic combustion [10], the combustion efficiency of 66% under nonequilibrium is much higher than the current value of 53.5% for the same fuel equivalence ratio of $\boldsymbol{\Phi} = 1.0$. This suggests that the inclusion of nonequilibrium air chemistry can exert more influence on hydrocarbon-fueled hypersonic combustion due to the lower reactivity and longer reaction chains.

As listed in Table 3, net thrusts have been achieved for the current examined high-Mach scramjet under both the equilibrium and nonequilibrium conditions. Although the boundary layer has been observably thickened along the inlet cowl surface under nonequilibrium because T_t is higher than T, the mass capture rate seems to be less influenced by the thermal nonequilibrium effect, and all the cases have nearly the same rate of 1.47 kg/s. The weak influence on air capture rate is because the growth of displacement thickness caused by nonequilibrium heating is not significant in the initial development stage of the boundary layer. However, the nonequilibrium heating induces observable displacement thickness in the boundary layer downstream of the inlet cowl, leading to higher pressure compression ratio. The isolator pressure, defined as the pressure at the entrance of the isolator section, is compressed from the ambient pressure of 433 Pa to be 24.85 and 25.33 kPa for the equilibrium and nonequilibrium cases, respectively. Note that the isolator pressure was not only determined by the inlet compression but also influenced by the intrusion of the upstream recirculation zone. The isolator pressure generally increases with the global fuel equivalence ratio, and higher values of 27.15 and 27.95 kPa are obtained for $\boldsymbol{\Phi} =$

Table 3 Overall engine performance under different equivalence ratios

Global performance	Equilibrium ($\Phi = 0.6$)	Nonequilibrium ($\Phi = 0.6$)	Nonequilibrium ($\Phi = 1.0$)	Nonequilibrium ($\Phi = 1.4$)
Air captured rate (kg/s)	1.47	1.47	1.47	1.47
Fuel flow rate (g/s)	60	60	100	140
Combustion efficiency	0.806	0.719	0.535	0.378
Isolator pressure (kPa)	24.85	25.33	27.15	27.95
Peak pressure ratio	5.26	4.16	4.90	4.48
Inviscid thrust (N)	890.07	864.72	883.83	938.38
Viscous drag (N)	527.02	471.48	454.30	347.88
Net thrust (N)	363.05	393.24	429.54	590.50
Specific impulse (s)	617.26	666.21	430.15	429.65

Downloaded by "Chinese Academy of Sciences (CAS), Institute of Mechanics" on April 11, 2024 | http://arc.aiaa.org | DOI: 10.2514/1.B39007

Downloaded by "Chinese Academy of Sciences (CAS), Institute of Mechanics" on April 11, 2024 | http://arc.aiaa.org | DOI: 10.2514/1.B39007

1.0 and 1.4, respectively. The equilibrium case under $\Phi = 0.6$ has the highest peak pressure ratio, which is defined as the ratio of peak pressure to the isolator pressure. The peak pressure ratio had a considerable 21% drop from 5.26 to 4.16 when the thermal nonequilibrium effect was taken into account. It is noted that the peak pressure ratio does not increase with the global equivalence ratio monotonically but achieves the highest value of 4.90 at $\Phi = 1.0$ for all the nonequilibrium cases. The inviscid thrust, i.e., the thrust produced by surface pressure on the engine walls, decreases from 890.07 to 864.72 N at $\Phi = 0.6$ with the presence of nonequilibrium. On the other hand, because the molecular viscosity associated with T_t is lower under nonequilibrium [29], the viscous drag due to friction also decreases from 527.02 to 471.48 N. The synchronous reductions in thrust and drag counteract each other and lead to a higher final net thrust of 393.24 N under nonequilibrium compared with the 363.05 N assuming equilibrium. This suggests that the drag reduction has a nonnegligible influence on the final net thrust compared with the improvement in combustion efficiency. The net thrust further increases under higher Φ for the nonequilibrium cases, but the specific impulse decreases reversely, implying that there exists an optimum fuel supply rate that can balance the thrust requirement and fuel economy. The current modeled specific impulses are consistent with the estimation considering the incomplete mixing effect [140], which estimated that the maximum specific impulse under Mach 10 should not exceed 800 s.

IV. Conclusions

An ethylene-fueled scramjet operating at Mach 10 is modeled by using IDDES to examine the influence of thermal/chemical nonequilibrium on engine performance. Grid convergence was verified by using five meshes with cell numbers from 79.31 million to 368.34 million. The scramjet modeled in this study was experimentally tested in the JF-24 detonation-driven pulse high-enthalpy shock tunnel, which can provide a stable test period of 16 ms. The thermal nonequilibrium was accounted for by the two-temperature model based on the Landau–Teller equation. The chemistry–vibration coupling is calculated by the combination of Park's model optimized by the QCT method and coupled vibration–chemistry–vibration (CVCV) model. To alleviate the huge computational cost of full-scale IDDES modeling with a 6.28-m-long domain and more than 100 million cells, zone-based models assuming local decoupling strategies are adopted. The thermal nonequilibrium is modeled by a zone-based nonequilibrium model (ZNM), and the turbulent combustion is modeled by a dynamic zone flamelet model (DZFM). An in-depth analysis of the effects of thermal and chemical nonequilibrium was conducted. The observations and revealed mechanisms would be useful in designing high-Mach scramjets to extend the operation limit of scramjets further.

This study reveals the contrary effects of nonequilibrium heating and nonequilibrium cooling due to the delayed relaxation of thermal nonequilibrium, which explains the seemingly contradictory observations of nonequilibrium effects in the literature. Generally, the nonequilibrium heating effect dominates in the compressing inlet, while the nonequilibrium cooling effect dominates in the divergent nozzle. The nonequilibrium heating thickens the boundary layer and may promote an early ignition, but the delayed rising of T_v tends to weaken the combustion reactions. The flame temperature under nonequilibrium is affected by the V-T energy exchange and the nonequilibrium chemistry, i.e., both the thermal and chemical nonequilibrium effects. The additional air dissociation and complication in reaction paths increase the probability of incomplete combustion, further reducing the flame temperature. The combustion is significantly suppressed under nonequilibrium, and the benefit of additional fuel when increasing the global fuel equivalence ratio cannot be fully released.

Quasi-one-dimensional performance analysis was compared for the equilibrium and nonequilibrium cases. Due to the reduced viscosity and strengthened flow turbulence under lower T_t, the nonequilibrium mixing is better than the equilibrium one. The final mixing efficiencies under $\Phi = 0.6$ are 86.7 and 83.0% for the equilibrium and nonequilibrium cases, respectively. Under nonequilibrium, the final mixing efficiency decreases to 69.2 and 55.2% as the global equivalence ratio is raised to 1.0 and 1.4, though with higher mixing efficiency, the final combustion efficiency of 72.5% under nonequilibrium is still lower than the 80.6% in the equilibrium case. Both the incorporation of nonequilibrium air chemistry and the nonequilibrium cooling effect contribute to the receding in reactivity. The combustion efficiency then decreases to 53.5 and 37.8% as the global fuel equivalence ratio increases from 0.6 to 1.0 and 1.4. The significant discrepancies of over 10% between the combustion and mixing efficiency indicate that the combustion is partially controlled by chemistry. The mass capture rate is less influenced by the thermal equilibrium effect because the boundary-layer displacement caused by nonequilibrium heating becomes prominent only after the inlet cowl, which eventually results in a higher pressure compression ratio. The synchronous reductions in thrust and drag counteract each other and lead to a higher final net thrust under nonequilibrium. Under realistic nonequilibrium conditions, the net thrust further increases under a higher equivalence ratio, whereas the specific impulse decreases.

The evolution of flamelets shows that intense combustion starts early before the fuel injectors. The abundant final products in the mixture fraction space indicate a more complete combustion in the equilibrium case, and the higher combustion efficiency from $x = 3.8$ to 5 m under nonequilibrium can be attributed to the good mixing. After incorporating the nonequilibrium air dissociation reactions, the peak concentrations of the O atom more than double, and the concentration of NO becomes comparable with the final products, implying that there are substantial endothermic dissociation reactions that significantly bring down the flame temperature. Reaction path analysis in the main reaction region shows that the abundance of OH radicals in the nonequilibrium case helps the pyrolysis of hydrocarbon fuels and the conversion from CO to CO_2, both of which raise the combustion efficiency over that of the equilibrium case from $x = 3.8$ to 5 m. Downstream of the man reaction region, the main difference between the reaction paths is that the nonequilibrium case has additional air dissociation reactions connected by OH. Nearly all the fuel has been converted into various oxides, e.g., CO, CO_2, and H_2O, in the postflame region before the nozzle. The conversion from CO to CO_2 is rate-limited by the OH in the equilibrium case, whereas it has reached a relatively stable status in the nonequilibrium case. With the reduction in temperature in the divergent nozzle, O and OH tend to recombine into O_2, while N and O recombine into NO. In general, the chemical nonequilibrium exerts more impact in the fuel-lean postflame regions, where the product dissociation has comparable path fluxes with the air dissociation. In the fuel-rich regions, the air dissociation reactions are much weaker than the intense combustion reactions, and the thermal nonequilibrium should take more effect through nonequilibrium heating/cooling as well as mixing enhancement.

Acknowledgments

The research was supported by National Key Research and Development Program of China (2021YFA0719204) and National Natural Science Foundation of China (12272387). The authors are grateful to the National Supercomputer Center in Tianjin for providing the computational resource.

References

[1] Stalker, R. J., and Morgan, R. G., "Free-Piston Shock Tunnel T4-Initial Operation and Preliminary Calibration," Univ. of Queensland, NASA CR-181721, Sept. 1988.

[2] Anderson, G., Kumar, A., and Erdos, J., "Progress in Hypersonic Combustion Technology with Computation and Experiment," AIAA Paper 1990-5254, 1990.

[3] Billig, F. S., and Dugger, G. L., "The Interaction of Shock Waves and Heat Addition in the Design of Supersonic Combustors," *Symposium (International) on Combustion*, Vol. 12, No. 1, 1969, pp. 1125–1139. https://doi.org/10.1016/S0082-0784(69)80490-X

Downloaded by "Chinese Academy of Sciences (CAS), Institute of Mechanics" on April 11, 2024 | http://arc.aiaa.org | DOI: 10.2514/1.B39007

[4] Ferri, A., "Review of Scramjet Propulsion Technology," *Journal of Aircraft*, Vol. 5, No. 1, 1968, pp. 3–10. https://doi.org/10.2514/3.43899

[5] Hank, J., Murphy, J., and Mutzman, R., "The X-51A Scramjet Engine Flight Demonstration Program," AIAA Paper 2008-2540, 2008. https://doi.org/10.2514/6.2008-2540

[6] Marshall, L. A., Bahm, C., Corpening, G. P., and Sherrill, R., "Overview with Results and Lessons Learned of the X-43A Mach 10 Flight," AIAA Paper 2005-3336, 2005.

[7] Smart, M. K., "How Much Compression Should a Scramjet Inlet Do?," *AIAA Journal*, Vol. 50, No. 3, 2012, pp. 610–619. https://doi.org/10.2514/1.j051281

[8] Yao, W., Liu, H., Xue, L., and Xiao, Y., "Performance Analysis of a Strut-Aided Hypersonic Scramjet by Full-Scale IDDES Modeling," *Aerospace Science and Technology*, Vol. 117, Oct. 2021, pp. 1–14. https://doi.org/10.1016/j.ast.2021.106941

[9] Yao, W., Liu, H., Li, L., and Yue, L., "Nonequilibrium Effect Modeling in High-Ma Scramjet Based on Dynamic Zone Model," AIAA Paper 2021-3543, 2021. https://doi.org/10.2514/6.2021-3543

[10] Yao, W., "Nonequilibrium Effects in Hypersonic Combustion Modeling," *Journal of Propulsion and Power*, Vol. 38, 2021, pp. 1–17.

[11] Liu, Y., He, X., Feng, L., Xue, R., Zhang, Y., Xu, C., and Du, J., "Numerical Simulation of the Interaction between Shock Train and Combustion in Three-Dimensional M12-02 Scramjet Model," *International Journal of Hydrogen Energy*, Vol. 47, No. 12, 2022, pp. 8026–8036. https://doi.org/10.1016/j.ijhydene.2021.12.126

[12] Kodera, M., Yang, V., Takahashi, M., and Itoh, K., "Ignition Transient Phenomena in a Scramjet Engine at Mach 12 Flight Condition," AIAA Paper 2007-5407, 2007. https://doi.org/10.2514/6.2007-5407

[13] Zhang, S., Li, J., Qin, F., Huang, Z., and Xue, R., "Numerical Investigation of Combustion Field of Hypervelocity Scramjet Engine," *Acta Astronautica*, Vol. 129, Dec. 2016, pp. 357–366. https://doi.org/10.1016/j.actaastro.2016.09.028

[14] Moura, A. F., Gibbons, N., Wheatley, V., McIntyre, T., and Jahn, I., "Characterization of Supersonic Turbulent Combustion in a Mach-10 Scramjet Combustor," *AIAA Journal*, Vol. 58, No. 5, 2020, pp. 2180–2196. https://doi.org/10.2514/1.J058671

[15] Wang, Y., Cheng, K., Tang, J., Liu, X., and Bao, W., "Analysis of the Maximum Flight Mach Number of Hydrocarbon-Fueled Scramjet Engines Under the Flight Cruising Constraint and the Combustor Cooling Requirement," *Aerospace Science and Technology*, Vol. 98, 2020, Paper 105594. https://doi.org/10.1016/j.ast.2019.105594

[16] Dudebout, R., Sislian, J. P., and Oppitz, R., "Numerical Simulation of Hypersonic Shock-Induced Combustion Ramjets," *Journal of Propulsion and Power*, Vol. 14, No. 6, 1998, pp. 869–879. https://doi.org/10.2514/2.5368

[17] Menees, G. P., Adelman, H. G., Cambier, J.-L., and Bowles, J. V., "Wave Combustors for Trans-Atmospheric Vehicles," *Journal of Propulsion and Power*, Vol. 8, No. 3, 1992, pp. 709–713. https://doi.org/10.2514/3.23536

[18] Alexander, D. C., and Sislian, J. P., "Computational Study of the Propulsive Characteristics of a Shcramjet Engine," *Journal of Propulsion and Power*, Vol. 24, No. 1, 2008, pp. 34–44. https://doi.org/10.2514/1.29951

[19] Chan, J., Sislian, J. P., and Alexander, D., "Numerically Simulated Comparative Performance of a Scramjet and Shcramjet at Mach 11," *Journal of Propulsion and Power*, Vol. 26, No. 5, 2010, pp. 1125–1134. https://doi.org/10.2514/1.48144

[20] Bricalli, M. G., Brown, L. M., and Boyce, R. R., "Supersonic Combustion Processes in a Premixed Three-Dimensional Nonuniform-Compression Scramjet Engine," *AIAA Journal*, Vol. 52, No. 8, 2014, pp. 1670–1685. https://doi.org/10.2514/1.J052640

[21] Petty, D. J., Wheatley, V., Smart, M. K., and Razzaqi, S. A., "Effects of Oxygen Enrichment on Scramjet Performance," *AIAA Journal*, Vol. 51, No. 1, 2013, pp. 226–235. https://doi.org/10.2514/1.J051732

[22] Barth, J. E., "Mixing and Combustion Enhancement in a Mach 12 Shape-Transitioning Scramjet Engine," Ph.D. Thesis, School of Mechanical and Mining Engineering, The Univ. of Queensland, 2014.

[23] Park, C., "Assessment of a Two-Temperature Kinetic Model for Dissociating and Weakly Ionizing Nitrogen," *Journal of Thermophysics and Heat Transfer*, Vol. 2, No. 1, 1988, pp. 8–16. https://doi.org/10.2514/3.55

[24] Hassan, B., Candler, G. V., and Olynick, D. R., "Thermo-Chemical Nonequilibrium Effects on the Aerothermodynamics of Aerobraking Vehicles," *Journal of Spacecraft and Rockets*, Vol. 30, No. 6, 1993, pp. 647–655. https://doi.org/10.2514/3.26369

[25] Knab, O., Fruehauf, H. H., and Messerschmid, E. W., "Theory and Validation of the Physically Consistent Coupled Vibration-Chemistry-Vibration Model," *Journal of Thermophysics and Heat Transfer*, Vol. 9, No. 2, 1995, pp. 219–226. https://doi.org/10.2514/3.649

[26] Fisher, E. M., "Calculations of the Effect of Nitrogen Vibrational Kinetics on Laminar Flame Temperature Profiles," *Combustion and Flame*, Vol. 108, Nos. 1–2, 1997, pp. 127–138.

[27] Hash, D., Olejniczak, J., Wright, M., Prabhu, D., Pulsonetti, M., Hollis, B., Gnoffo, P., Barnhardt, M., Nompelis, I., and Candler, G., "Fire Ii Calculations for Hypersonic Nonequilibrium Aerothermodynamics Code Verification: Dplr, Laura, and Us3d," AIAA Paper 2007-605, 2007. https://doi.org/10.2514/6.2007-605

[28] Farbar, E., Boyd, I. D., and Martin, A., "Numerical Prediction of Hypersonic Flowfields Including Effects of Electron Translational Nonequilibrium," *Journal of Thermophysics and Heat Transfer*, Vol. 27, No. 4, 2013, pp. 593–606. https://doi.org/10.2514/1.T3963

[29] Koo, H., Raman, V., and Varghese, P. L., "Direct Numerical Simulation of Supersonic Combustion with Thermal Nonequilibrium," *Proceedings of the Combustion Institute*, Vol. 35, No. 2, 2015, pp. 2145–2153. https://doi.org/10.1016/j.proci.2014.08.005

[30] Casseau, V., Palharini, R. C., Scanlon, T. J., and Brown, R. E., "A Two-Temperature Open-Source CFD Model for Hypersonic Reacting Flows, Part One: Zero-Dimensional Analysis," *Aerospace*, Vol. 3, No. 34, 2016, pp. 1–21. https://doi.org/10.3390/aerospace3040034

[31] Fiévet, R., Voelkel, S., Koo, H., Raman, V., and Varghese, P. L., "Effect of Thermal Nonequilibrium on Ignition in Scramjet Combustors," *Proceedings of the Combustion Institute*, Vol. 36, No. 2, 2017, pp. 2901–2910. https://doi.org/10.1016/j.proci.2016.08.066

[32] Casseau, V., "An Open-Source CFD Solver for Planetary Entry," Ph.D. Thesis, Dept. of Mechanical and Aerospace Engg., Univ. of Strathclyde, 2017.

[33] Wang, J., Lin, W., Huang, W., Shi, Q., and Zhao, J., "Numerical Study on Atomization and Evaporation Characteristics of Preheated Kerosene Jet in a Rotating Detonation Scramjet Combustor," *Applied Thermal Engineering*, Vol. 203, Feb. 2022, Paper 117920. https://doi.org/10.1016/j.applthermaleng.2021.117920

[34] Yao, W., "Kerosene-Fueled Supersonic Combustion Modelings Based on Skeletal Mechanisms," *Acta Mechanica Sinica*, Vol. 35, Sept. 2019, pp. 1155–1177. https://doi.org/10.1007/s10409-019-00891-w

[35] Yao, W., Lu, Y., Wu, K., Wang, J., and Fan, X., "Modeling Analysis of an Actively-Cooled Scramjet Combustor Under Different Kerosene/Air Ratios," *Journal of Propulsion and Power*, Vol. 34, No. 4, 2018, pp. 975–991. https://doi.org/10.2514/1.B36866

[36] Ogawa, S., Kobayashi, K., and Tomioka, S., "Study on the Ignition Method for n-Octane Pyrolysis Fuel in a Scramjet Engine," *Transactions of the Japan Society for Aeronautical and Space Sciences*, Vol. 65, No. 1, 2022, pp. 33–43. https://doi.org/10.2322/tjsass.65.33

[37] Stalker, R., "Thermodynamics and Wave Processes in High Mach Number Propulsive Ducts," AIAA Paper 1989-0261, 1989. https://doi.org/10.2514/6.1989-261

[38] Xi, Z., Gao, Y., Liu, M., and Zhang, H., "Control-Oriented Quasi-One Dimensional Modeling Method for Scramjet," *International Journal of Turbo & Jet-Engines*, April 2021, Paper 000010151520210004. https://doi.org/10.1515/tjeng-2021-0004

[39] Li, J., Jiang, Z., Chen, H., Feng, H., and Yu, H., "Numerical Study on Backward-Forward Double-Detination Driver for High Enthalpy Shock Tubes," *Chinese Journal of Theoretical and Applied Mechanics*, Vol. 39, No. 3, 2007, pp. 343–349. https://doi.org/10.6052/0459-1879-2007-3-2005-432

[40] Jiang, Z., "Experiments and Development of Long-Test-Duration Hypervelocity Detonation-Driven Shock Tunnel (LHDst)," *52nd Aerospace Sciences Meeting*, AIAA Paper 2014-1012, 2014. https://doi.org/10.2514/6.2014-1012

[41] Yu, H. R., Chen, H., and Zhao, W., "Advances in Detonation Driving Techniques for a Shock Tube/Tunnel," *Shock Waves*, Vol. 15, No. 6, 2006, pp. 399–405. https://doi.org/10.1007/s00193-006-0041-2

Downloaded by "Chinese Academy of Sciences (CAS), Institute of Mechanics" on April 11, 2024 | http://arc.aiaa.org | DOI: 10.2514/1.B39007

[42] Wang, Y., Hu, Z., Liu, Y., and Jiang, Z., "Starting Process in a Large-Scale Shock Tunnel," *AIAA Journal*, Vol. 54, No. 4, 2016, pp. 1240–1249.
https://doi.org/10.2514/1.J054145

[43] Molder, S., and Szpiro, E. J., "Busemann Inlet for Hypersonic Speeds," *Journal of Spacecraft and Rockets*, Vol. 3, No. 8, 1966, pp. 1303–1304.
https://doi.org/10.2514/3.28649

[44] Saarlas, M., "Reference Temperature Method for Computing Displacement Thickness," *AIAA Journal*, Vol. 2, No. 11, 1964, pp. 2056–2057.
https://doi.org/10.2514/3.2741

[45] Yao, W., Wu, K., and Fan, X., "Development of Skeletal Kerosene Mechanisms and Application to Supersonic Combustion," *Energy & Fuels*, Vol. 32, No. 12, 2018, pp. 12,992–13,003.
https://doi.org/10.1021/acs.energyfuels.8b03350

[46] Nakaya, S., Kinoshita, R., Lee, J., Ishikawa, H., and Tsue, M., "Analysis of Supersonic Combustion Characteristics of Ethylene/Methane Fuel Mixture on High-Speed Measurements of CH* Chemiluminescence," *Proceedings of the Combustion Institute*, Vol. 37, No. 3, 2019, pp. 3749–3756.
https://doi.org/10.1016/j.proci.2018.09.011

[47] Kannaiyan, K., "Computational Study of the Effect of Cavity Geometry on the Supersonic Mixing and Combustion of Ethylene," *Journal of Computational Science*, Vol. 47, Nov. 2020, Paper 101243.
https://doi.org/10.1016/j.jocs.2020.101243

[48] Li, P., Wang, H., Sun, M., Liu, C., and Li, F., "Numerical Study on the Mixing and Evaporation Process of a Liquid Kerosene Jet in a Scramjet Combustor," *Aerospace Science and Technology*, Vol. 119, Dec. 2021, Paper 107095.
https://doi.org/10.1016/j.ast.2021.107095

[49] Wang, Z.-G., Sun, M.-B., Wang, H.-B., Yu, J.-F., Liang, J.-H., and Zhuang, F.-C., "Mixing-Related Low Frequency Oscillation of Combustion in an Ethylene-Fueled Supersonic Combustor," *Proceedings of the Combustion Institute*, Vol. 35, No. 2, 2015, pp. 2137–2144.
https://doi.org/10.1016/j.proci.2014.09.005

[50] Boles, J. A., Choi, J.-I., Edwards, J. R., and Baurle, R. A., "Simulations of High-Speed Internal Flows Using LES/RANS Models," AIAA Paper 2009-1324, 2009.
https://doi.org/10.2514/6.2009-1324

[51] Saghafian, A., Shunn, L., Philips, D. A., and Ham, F., "Large Eddy Simulations of the HIFiRE Scramjet Using a Compressible Flamelet/Progress Variable Approach," *Proceedings of the Combustion Institute*, Vol. 35, No. 2, 2015, pp. 2163–2172.
https://doi.org/10.1016/j.proci.2014.10.004

[52] Hass, N., Cabell, K., and Storch, A., "HIFiRE Direct-Connect Rig (HDCR) Phase I Scramjet Test Results from the NASA Langley Arc-Heated Scramjet Test Facility," AIAA Paper 2011-2248, 2011.
https://doi.org/10.2514/6.2011-2248

[53] Cheng, D., Wang, J., Lu, Y., Li, L., Yao, W., and Fan, X., "Wall Heat Flux Measurements for a Kerosene-Fueled Supersonic Combustor," *Journal of Aerospace Engineering*, Vol. 32, No. 5, 2019, Paper 04019080.
https://doi.org/10.1061/(ASCE)AS.1943-5525.0001076

[54] Spalding, D. B., "A Single Formula for 'Law of the Wall'," *Journal of Applied Mechanics*, Vol. 28, No. 3, 1961, pp. 455–458.
https://doi.org/10.1115/1.3641728

[55] Villiers, E. D., "The Potential of Large Eddy Simulation for the Modeling of Wall Bounded Flows," Ph.D. Thesis, Dept. of Mechanical Engineering, Imperial College London, 2006.

[56] Fureby, C., "LES for Supersonic Combustion," *18th AIAA/3af International Space Planes and Hypersonic Systems and Technologies Conference*, AIAA Paper 2012-5979, 2012.

[57] Li, Q., and Wang, Z., "Dynamic Mode Decomposition of Turbulent Combustion Process in DLR Scramjet Combustor," *Journal of Aerospace Engineering*, Vol. 30, No. 5, 2017, Paper 4017034.
https://doi.org/10.1061/(asce)as.1943-5525.0000747

[58] Huang, Z.-W., He, G.-Q., Qin, F., and Wei, X.-G., "Large Eddy Simulation of Flame Structure and Combustion Mode in a Hydrogen Fueled Supersonic Combustor," *International Journal of Hydrogen Energy*, Vol. 40, No. 31, 2015, pp. 9815–9824.
https://doi.org/10.1016/j.ijhydene.2015.06.011

[59] Steiner, H., and Bushe, W. K., "Large Eddy Simulation of a Turbulent Reacting Jet with Conditional Source-Term Estimation," *Physics of Fluids*, Vol. 13, 2001, pp. 754–769.

[60] Pitsch, H., Wan, Y. P., and Peters, N., "Numerical Investigation of Soot Formation and Oxidation Under Diesel Engine Conditions," *Fuels & Lubricants Meeting & Exposition*, SAE International Paper SAE 952357, Oct. 1995.
https://doi.org/10.4271/952357

[61] Oijen, J. A. V., and Goey, L. P. H. D., "Modelling of Premixed Laminar Flames Using Flamelet-Generated Manifolds," *Combustion Science and Technology*, Vol. 161, No. 1, 2000, pp. 113–137.
https://doi.org/10.1080/00102200008935814

[62] Mittal, V., Cook, D. J., and Pitsch, H., "An Extended Multi-Regime Flamelet Model for IC Engines," *Combustion and Flame*, Vol. 159, No. 8, 2012, pp. 2767–2776.
https://doi.org/10.1016/j.combustflame.2012.01.014

[63] Gao, Z., Jiang, C., and Lee, C.-H., "Representative Interactive Flamelet Model and Flamelet/Progress Variable Model for Supersonic Combustion Flows," *Proceedings of the Combustion Institute*, Vol. 36, No. 2, 2017, pp. 2937–2946.
https://doi.org/10.1016/j.proci.2016.06.184

[64] Jesse, Q., Tomasz, G. D., James, C. M., Guilhem, L., and Joseph, C. O., "A Priori Analysis of a Compressible Flamelet Model Using RANS Data for a Dual-Mode Scramjet Combustor," AIAA Paper 2015-3208, 2015.
https://doi.org/10.2514/6.2015-3208

[65] Gritskevich, M. S., Garbaruk, A. V., Schütze, J., and Menter, F. R., "Development of DDES and IDDES Formulations for the K-Ω Shear Stress Transport Model," *Flow Turbulence and Combustion*, Vol. 3, Nov. 2012, pp. 1–19.
https://doi.org/10.1007/s10494-011-9378-4

[66] Choi, H., and Moin, P., "Grid-Point Requirements for Large Eddy Simulation: Chapman's Estimates Revisited," *Physics of Fluids*, Vol. 24, No. 1, 2012, pp. 011702.1–011702.5.
https://doi.org/10.1063/1.3676783

[67] Bose, S. T., and Park, G. I., "Wall-Modeled Large-Eddy Simulation for Complex Turbulent Flows," *Annual Review of Fluid Mechanics*, Vol. 50, Jan. 2018, pp. 535–561.
https://doi.org/10.1146/annurev-fluid-122316-045241

[68] Shur, M. L., Spalart, P. R., Strelets, M. K., and Travin, A. K., "A Hybrid RANS-LES Approach with Delayed-DES and Wall-Modelled LES Capabilities," *International Journal of Heat and Fluid Flow*, Vol. 29, No. 6, 2008, pp. 1638–1649.
https://doi.org/10.1016/j.ijheatfluidflow.2008.07.001

[69] Tominaga, Y., and Stathopoulos, T., "Turbulent Schmidt Numbers for CFD Analysis with Various Types of Flowfield," *Atmospheric Environment*, Vol. 41, No. 37, 2007, pp. 8091–8099.
https://doi.org/10.1016/j.atmosenv.2007.06.054

[70] Baurle, R. A., and Eklund, D. R., "Analysis of Dual-Mode Hydrocarbon Scramjet Operation at Mach 4–6.5," *Journal of Propulsion and Power*, Vol. 18, No. 5, 2002, pp. 990–1002.
https://doi.org/10.2514/2.6047

[71] Sturgess, G. J., and McManus, K. R., "Calculations of Turbulent Mass Transport in a Bluff-Body Diffusion-Flame Combustor," AIAA Paper 1984-0372, 1984.

[72] Ott, J. D., Brinckman, C. K. K., and Dash, S. M., "Scramjet Propulsive Flowpath Prediction Improvements Using Recent Modeling Upgrades," *43rd Aerospace Sciences Meeting and Exhibition*, AIAA Paper 2005-0432, Jan. 2005.

[73] Antonia, R. A., "Behaviour of the Turbulent Prandtl Number near the Wall," *International Journal of Heat and Mass Transfer*, Vol. 23, No. 6, 1980, pp. 906–908.

[74] Keistler, P., "Simulation of Supersonic Combustion Using Variable Turbulent Prandtl/Schmidt Numbers Formulation," Ph.D. Thesis, Dept. of Mechanical and Aerospace Engg., North Carolina State Univ., 2006.

[75] Baurle, R. A., and Edwards, J. R., "Hybrid Reynolds-Averaged/Large-Eddy Simulations of a Coaxial Supersonic Freejet Experiment," *AIAA Journal*, Vol. 48, No. 3, 2010, pp. 551–571.
https://doi.org/10.2514/1.43771

[76] Steiner, H., Irrenfried, C., and Brenn, G., "Near-Wall Determination of the Turbulent Prandtl Number Based on Experiments, Numerical Simulation and Analytical Models," *Heat Transfer Engineering*, Vol. 41, Nos. 15–16, 2019, pp. 1341–1353.
https://doi.org/10.1080/01457632.2019.1628483

[77] Kays, W. M., "Turbulent Prandtl Number—Where Are We?" *Journal of Heat Transfer*, Vol. 116, No. 2, 1994, pp. 284–295.
https://doi.org/10.1115/1.2911398

[78] Weller, H. G., Tabor, G., Jasak, H., and Fureby, C., "A Tensorial Approach to Computational Continuum Mechanics Using Object-Oriented Techniques," *Computers in Physics*, Vol. 12, No. 6, 1998, pp. 620–631.

[79] Peterson, D. M., and Hassan, E. A., "Hybrid RANS/LES of Combustion in a Supersonic Cavity Flameholder at Mach 2 and Mach 3," *2018 AIAA Aerospace Sciences Meeting*, AIAA Paper 2018-1144, 2018.

[80] Vreman, B., Geurts, B., and Kuerten, H., "Subgrid-Modeling in LES of Compressible Flow," *Applied Scientific Research*, Vol. 54, No. 3, 1995,

pp. 191–203.
https://doi.org/10.1007/BF00849116
[81] Moin, P., Squires, K., Cabot, W., and Lee, S., "A Dynamic Subgrid-Scale Model for Compressible Turbulence and Scalar Transport," *Physics of Fluids A: Fluid Dynamics*, Vol. 3, Sept. 1991, pp. 2746–2757.
https://doi.org/10.1063/1.858164
[82] Ribert, G., Petit, X., and Domingo, P., "High-Pressure Methane-Oxygen Flames: Analysis of Sub-Grid Scale Contributions in Filtered Equations of State," *Journal of Supercritical Fluids*, Vol. 121, March 2017, pp. 78–88.
https://doi.org/10.1016/j.supflu.2016.08.020
[83] Wang, X., Huo, H., Unnikrishnan, U., and Yang, V., "A Systematic Approach to High-Fidelity Modeling and Efficient Simulation of Supercritical Fluid Mixing and Combustion," *Combustion and Flame*, Vol. 195, Sept. 2018, pp. 203–215.
https://doi.org/10.1016/j.combustflame.2018.04.030
[84] Müller, H., Niedermeier, C. A., Matheis, J., Pfitzner, M., and Hickel, S., "Large-Eddy Simulation of Nitrogen Injection at Trans- and Supercritical Conditions," *Physics of Fluids*, Vol. 28, No. 1, 2016, pp. 015102.1–015102.28.
https://doi.org/10.1063/1.4937948
[85] Müller, H., Pfitzner, M., Matheis, J., and Hickel, S., "Large-Eddy Simulation of Coaxial LN2/GH2 Injection at Trans- and Supercritical Conditions," *Journal of Propulsion and Power*, Vol. 32, No. 1, 2015, pp. 1–11.
https://doi.org/10.2514/1.B35827
[86] Schmitt, T., Méry, Y., Boileau, M., and Candel, S., "Large-Eddy Simulation of Oxygen/Methane Flames Under Transcritical Conditions," *Proceedings of the Combustion Institute*, Vol. 33, No. 1, 2011, pp. 1383–1390.
https://doi.org/10.1016/j.proci.2010.07.036
[87] Lapenna, P. E., Indelicato, G., Lamioni, R., and Creta, F., "Modeling the Equations of State Using a Flamelet Approach in LRE-Like Conditions," *Acta Astronautica*, Vol. 158, May 2019, pp. 460–469.
https://doi.org/10.1016/j.actaastro.2018.07.025
[88] Ke, H.-B., and He, Y.-L., "The Mechanisms of Thermal Diffusion and Baro-Diffusion Effects on Thermacoustic Mixture Separation," *Chemical Engineering Science*, Vol. 84, Dec. 2012, pp. 399–407.
https://doi.org/10.1016/j.ces.2012.08.021
[89] Palle, S., Nolan, C., and Millera, R. S., "On Molecular Transport Effects in Real Gas Laminar Diffusion Flames at Large Pressure," *Physic of Fluids*, Vol. 17, Oct. 2005, pp. 1–19.
[90] Curtis, E. W., and Farrell, P. V., "A Numerical Study of High-Pressure Droplet Vaporization," *Combustion and Flame*, Vol. 90, No. 2, 1992, pp. 85–102.
https://doi.org/10.1016/0010-2180(92)90111-2
[91] Yao, W., "On the Application of Dynamic Zone Flamelet Model to Large Eddy Simulation of Supersonic Hydrogen Flame," *International Journal of Hydrogen Energy*, Vol. 45, No. 41, 2020, pp. 21,940–21,955.
https://doi.org/10.1016/j.ijhydene.2020.05.189
[92] Bilger, R. W., "Conditional Moment Closure Modelling and Advanced Laser Measurements," *Turbulence and Molecular Processes in Combustion*, Elsevier, Amsterdam, Oct. 1992, pp. 267–287.
[93] Salehi, F., Talei, M., Hawkes, E. R., Bhagatwala, A., Chen, J. H., Yoo, C. S., and Kook, S., "Doubly Conditional Moment Closure Modelling for HCCI with Temperature Inhomogeneities," *Proceedings of the Combustion Institute*, Vol. 36, No. 3, 2017, pp. 3677–3685.
https://doi.org/10.1016/j.proci.2016.05.021
[94] Klimenko, A. Y., and Pope, S. B., "The Modeling of Turbulent Reactive Flows Based on Multiple Mapping Conditioning," *Physics of Fluids*, Vol. 15, No. 7, 2003, pp. 1907–1925.
https://doi.org/10.1063/1.1575754
[95] Vogiatzaki, K., Kronenburg, A., Cleary, M. J., and Kent, J. H., "Multiple Mapping Conditioning of Turbulent Jet Diffusion Flames," *Proceedings of the Combustion Institute*, Vol. 32, No. 2, 2009, pp. 1679–1685.
https://doi.org/10.1016/j.proci.2008.06.164
[96] Klimenkoa, A. Y., and Bilger, R. W., "Conditional Moment Closure for Turbulent Combustion," *Progress in Energy and Combustion Science*, Vol. 25, Dec. 1999, pp. 595–687.
https://doi.org/10.1016/S0360-1285(99)00006-4
[97] Thornber, B., Bilger, R. W., Masri, A. R., and Hawkes, E. R., "An Algorithm for LES of Premixed Compressible Flows Using the Conditional Moment Closure Model," *Journal of Computational Physics*, Vol. 230, No. 20, 2011, pp. 7687–7705.
https://doi.org/10.1016/j.jcp.2011.06.024
[98] Sitte, M. P., and Mastorakos, E., "Modelling of Spray Flames with Doubly Conditional Moment Closure," *Flow Turbul Combust*, Vol. 99, No. 3, 2017, pp. 933–954.
https://doi.org/10.1007/s10494-017-9873-3
[99] Zettervall, N., Fureby, C., and Nilsson, E. J. K., "Small Skeletal Kinetic Reaction Mechanism for Ethylene–Air Combustion," *Energy & Fuels*, Vol. 31, No. 12, 2017, pp. 14,138–14,149.
https://doi.org/10.1021/acs.energyfuels.7b02078
[100] Masri, A. R., Dibble, R. W., and Barlow, R. S., "The Structure of Turbulent Nonpremixed Flames of Methanol over a Range of Mixing Rates," *Combustion and Flame*, Vol. 89, May 1992, pp. 167–185.
https://doi.org/10.1016/0010-2180(92)90026-L
[101] Park, C., "The Limits of Two-Temperature Model," AIAA Paper 2010-911, 2010.
https://doi.org/10.2514/6.2010-911
[102] Han, S., Lee, S., and Lee, B. J., "Numerical Analysis of Thermochemical Nonequilibrium Flows in a Model Scramjet Engine," *Energies*, Vol. 13, No. 3, 2020, pp. 606–623.
https://doi.org/10.3390/en13030606
[103] Bird, G. A., *The DSMC Method*, CreateSpace Independent Publishing Platform, Charleston, 2013, pp. 49–66.
[104] Millikan, R. C., and White, D. R., "Systematics of Vibrational Relaxation," *Journal of Chemical Physics*, Vol. 39, No. 12, 1963, pp. 3209–3213.
https://doi.org/10.1063/1.1734182
[105] Landau, L., and Teller, E., "On the Theory of Sound Dispersion," *Collected Papers of L. D. Landau*, Pergamon Press, Oxford, 1965, pp. 147–153.
[106] Park, C., "Review of Chemical-Kinetic Problems of Future NASA Missions. I–Earth Entries," *Journal of Thermophysics and Heat Transfer*, Vol. 7, No. 3, 1993, pp. 385–398.
https://doi.org/10.2514/3.431
[107] Voelkel, S., Raman, V., and Varghese, P. L., "Effect of Thermal Nonequilibrium on Reactions in Hydrogen Combustion," *Shock Waves*, Vol. 26, No. 5, 2016, pp. 539–549.
https://doi.org/10.1007/s00193-016-0645-0
[108] Knab, O., Gogel, T. H., Fruhauf, H. H., and Messerschmid, E. W., "CVCV-Model Validation by Means of Radiative Heating Calculations," AIAA Paper 1995-0623, 1995.
https://doi.org/10.2514/6.1995-623
[109] Gnoffo, P. A., Gupta, R. N., and Shinn, J. L., "Conservation Equations and Physical Models for Hypersonic Air Flows in Thermal and Chemical Nonequilibrium," NASA TP-2867, Hampton, VA, Feb. 1989.
[110] Yao, W., Wang, J., Lu, Y., Li, X., and Fan, X., "Full-Scale Detached Eddy Simulation of Kerosene Fueled Scramjet Combustor Based on Skeletal Mechanism," AIAA Paper 2015-3579, 2015.
https://doi.org/10.2514/6.2015-3579
[111] Wu, K., Zhang, P., Yao, W., and Fan, X., "Numerical Investigation on Flame Stabilization in DLR Hydrogen Supersonic Combustor with Strut Injection," *Combustion Science and Technology*, Vol. 189, No. 12, 2017, pp. 2154–2179.
https://doi.org/10.1080/00102202.2017.1365847
[112] Yao, W., Lu, Y., Li, X., Wang, J., and Fan, X., "Improved Delayed Detached Eddy Simulation of a High-Ma Active-Cooled Scramjet Combustor Based on Skeletal Kerosene Mechanism," AIAA Paper 2016-4761, 2016.
https://doi.org/10.2514/6.2016-4761
[113] Yao, W., Yuan, Y., Li, X., Wang, J., Wu, K., and Fan, X., "Comparative Study of Elliptic and Round Scramjet Combustors Fueled by RP-3," *Journal of Propulsion and Power*, Vol. 34, No. 3, 2018, pp. 772–786.
https://doi.org/10.2514/1.B36721
[114] Wu, K., Yao, W., and Fan, X., "Development and Fidelity Evaluation of a Skeletal Ethylene Mechanism Under Scramjet-Relevant Conditions," *Energy & Fuels*, Vol. 31, No. 12, 2017, pp. 14,296–14,305.
https://doi.org/10.1021/acs.energyfuels.7b03033
[115] Yao, W., Wu, K., and Fan, X., "Influences of Domain Symmetry on Supersonic Combustion Modeling," *Journal of Propulsion and Power*, Vol. 35, No. 2, 2019, pp. 451–465.
https://doi.org/10.2514/1.B37227
[116] Weller, H. G., Tabor, G., Jasak, H., and Fureby, C., "A Tensorial Approach to CFD Using Object Oriented Techniques," *Computers in Physics*, Vol. 12, No. 6, 1997, pp. 620–631.
https://doi.org/10.1063/1.168744
[117] Salehi, F., Talei, M., Hawkes, E. R., Yoo, C. S., Lucchini, T., D'Errico, G., and Kook, S., "Conditional Moment Closure Modelling for Hcci with Temperature Inhomogeneities," *Proceedings of the Combustion Institute*, Vol. 35, No. 3, 2015, pp. 3087–3095.
https://doi.org/10.1016/j.proci.2014.05.035
[118] Wu, K., Contino, F., Yao, W., and Fan, X., "On the Application of Tabulated Dynamic Adaptive Chemistry in Ethylene-Fueled Supersonic Combustion," *Combustion and Flame*, Vol. 197, Nov. 2018,

Downloaded by "Chinese Academy of Sciences (CAS), Institute of Mechanci" on April 11, 2024 | http://arc.aiaa.org | DOI: 10.2514/1.B39007

pp. 265–275.
https://doi.org/10.1016/j.combustflame.2018.08.012
[119] Lee, Y., Yao, W., and Fan, X., "Low-Dissipative Hybrid Compressible Solver Designed for Large Eddy Simulation of Supersonic Turbulent Flows," *AIAA Journal*, Vol. 56, No. 8, 2018, pp. 3086–3096.
https://doi.org/10.2514/1.J056404
[120] Chen, S.-S., Yan, C., and Xiang, X.-H., "Effective Low-Mach Number Improvement for Upwind Schemes," *Computers & Mathematics with Applications*, Vol. 75, No. 10, 2018, pp. 3737–3755.
https://doi.org/10.1016/j.camwa.2018.02.028
[121] Greenshields, C. J., Weller, H. G., Gasparini, L., and Reese, J. M., "Implementation of Semi-Discrete, Non-Staggered Central Schemes in a Colocated, Polyhedral, Finite Volume Framework, for High-Speed Viscous Flows," *International Journal for Numerical Methods in Fluids*, Vol. 38, No. 2, 2009, pp. 139–161.
https://doi.org/10.1002/fld.2069
[122] Kurganov, A., Noelle, S., and Petrova, G., "Semidiscrete Central-Upwind Schemes for Hyperbolic Conservation Laws and Hamilton-Jacobi Equations," *SIAM Journal on Scientific Computing*, Vol. 23, No. 3, 2001, pp. 707–740.
https://doi.org/10.1137/S1064827500373413
[123] Pirozzoli, S., "Generalized Conservative Approximations of Split Convective Derivative Operators," *Journal of Computational Physics*, Vol. 229, No. 19, 2010, pp. 7180–7190.
https://doi.org/10.1016/j.jcp.2010.06.006
[124] Vuorinen, V., Larmi, M., Schlatter, P., Fuchs, L., and Boersma, B. J., "A Low-Dissipative, Scale-Selective Discretization Scheme for the Navier–Stokes Equations," *Computers & Fluids*, Vol. 70, Nov. 2012, pp. 195–205.
https://doi.org/10.1016/j.compfluid.2012.09.022
[125] Crank, J., and Nicotson, P., "A Practical Method for Numerical Evaluation of Solutions of Partial Differential Equations of the Heat-Conduction Type," *Advances in Computational Mathematics*, Vol. 6, Jan. 1996, pp. 207–226.
https://doi.org/10.1007/BF02127704
[126] Blottner, F. G., Johnson, M., and Ellis, M., "Chemically Reacting Viscous Flow Program for Multi-Component Gas Mixtures," SC-RR-70-754, Sandia Laboratories, Albuquerque, NM, Dec. 1971.
[127] Vincenti, W. G., and Kruger, C. H., *Introduction to Physical Gas Dynamics*, Krieger, New York, 1975, p. 21.
[128] Gupta, R. N., Lee, K.-P., Thompson, R. A., and Yos, J. M., "Calculations and Curve Fits of Thermodynamics and Transport Properties for Equilibrium Air to 30000 K," NASA RP 1260, Oct. 1991.
[129] Kee, R. J., Rupley, F. M., and Miller, J. A., "CHEMKIN-Ii: A Fortran Chemical Kinetics Package for the Analysis of Gas-Phase Chemical Kinetics," SAND-89-8009, Sandia National Laboratories, Livermore, CA, Sept. 1989.
[130] Bird, R. B., Stewart, W. E., and Lightfoot, E. N., "Viscosity and the Mechanisms of Momentum Transport," *Transport Phenomena*, 2nd ed., Wiley, New York, 2002, p. 27.
[131] Wilke, C. R., "A Viscosity Equation for Gas Mixtures," *Journal of Chemical Physics*, Vol. 18, No. 4, 1950, pp. 517–519.
https://doi.org/10.1063/1.1747673
[132] Mathur, S., Tondon, P. K., and Saxena, S. C., "Thermal Conductivity of Binary, Ternary and Quaternary Mixtures of Rare Gases," *Molecular Physics*, Vol. 12, No. 6, 1967, pp. 569–579.
https://doi.org/10.1080/00268976700100731
[133] Sutton, K., and Gnoffo, P., "Multi-Component Diffusion with Application to Computational Aerothermodynamics," AIAA Paper 1998-2575, 1998.
https://doi.org/10.2514/6.1998-2575
[134] Yuan, Y., Zhang, T., Yao, W., and Fan, X., "Study on Flame Stabilization in a Dual-Mode Combustor Using Optical Measurements," *Journal of Propulsion and Power*, Vol. 31, No. 6, 2015, pp. 1524–1531.
https://doi.org/10.2514/1.b35689
[135] Barth, J. E., Wheatley, V., and Smart, M. K., "Effects of Hydrogen Fuel Injection in a Mach 12 Scramjet Inlet," *AIAA Journal*, Vol. 53, No. 10, 2015, pp. 2907–2919.
https://doi.org/10.2514/1.J053819
[136] Law, C. K., "Oxidation Mechanisms of Fuels," *Combustion Physics*, Cambridge Univ. Press, Cambridge, England, U.K., 2006, pp. 84–137.
[137] Warnatz, J., "The Structure of Laminar Alkane-, Alkene-, and Acetylene Flames," *Symposium (International) on Combustion*, Vol. 18, No. 1, 1981, pp. 369–384.
[138] Lindstedt, P., "Modeling of the Chemical Complexities of Flames," *Symposium (International) on Combustion*, Vol. 27, No. 1, 1998, pp. 269–285.
[139] Ingenito, A., Cecere, D., and Giacomazzi, E., "Large Eddy Simulation of Turbulent Hydrogen-Fuelled Supersonic Combustion in an Air Cross-Flow," *Shock Waves*, Vol. 23, No. 5, 2013, pp. 481–494.
https://doi.org/10.1007/s00193-013-0454-7
[140] Sislian, J. P., Dudebout, R., Schumacher, J., Islam, M., and Redford, T., "Incomplete Mixing and Off-Design Effects on Shock-Induced Combustion Ramjet Performance," *Journal of Propulsion and Power*, Vol. 16, No. 1, 2000, pp. 41–48.
https://doi.org/10.2514/2.5529

J. C. Oefelein
Associate Editor

Downloaded by "Chinese Academy of Sciences (CAS), Institute of Mechanics" on April 11, 2024 | http://arc.aiaa.org | DOI: 10.2514/1.B39007

This article has been cited by:

1. Hang Liu, Wei Yao, Xu Zhang, Xiaoyuan Zhang, Jianwen Liu, Lianjie Yue, Quanhua Sun. Nonequilibrium Heating/Cooling Effects in a Mach Number 10 Hydrogen-Fueled Scramjet. *Journal of Propulsion and Power*, ahead of print1-17. [Abstract] [Full Text] [PDF] [PDF Plus]
2. Zheng Zhang, Wei Yao, Qiu Wang, Wei Zhao. 2023. IDDES simulation of hydrogen-fueled supersonic combustion based on dynamic zone flamelet model. *Fuel* **347**, 128502. [Crossref]

Downloaded by "Chinese Academy of Sciences (CAS), Institute of Mechancis" on April 11, 2024 | http://arc.aiaa.org | DOI: 10.2514/1.B39007